In Vitro Modelling of Fuchs Endothelial Dystrophy for Corneal Endothelial Cell Apoptosis and Characterization of Human Descemet's Membrane

by

Myagmartsend Enkhbat

A thesis

presented to the University of Waterloo

in fulfillment of the

thesis requirement for the degree of

Master of Applied Science

in

Chemical Engineering

Waterloo, Ontario, Canada, 2024

© Myagmartsend Enkhbat 2024

AUTHOR'S DECLARATION

This thesis consists of material all of which I authored or co-authored: see Statement of Contributions included in the thesis. This is a true copy of the thesis, including any required final revisions, as accepted by my examiners.

I understand that my thesis may be made electronically available to the public.

STATEMENT OF CONTRIBUTIONS

Chapter 3 and Chapter 4 consists of the reanalyzed raw data from Deepak Jain from the Department of Chemical Engineering, University of Waterloo (Annexin V and PI for immunostaining and TUNEL assay) and Wesley Luu from the Department of Chemical Engineering, University of Waterloo (Annexin V and PI for immunostaining, TUNEL assay, α-SMA, and Descemet's Membrane stiffness measurements). Chapter 1, section 1.2.4 are from a review paper I co-authored with Fancheng Sun from the Department of Chemical Engineering, University of Waterloo. The human Descemet's membrane tissue samples used in Chapter 4 were received from Prof. Jodhbir S Mehta and Dr. Gary S. L. Peh at Singapore Eye Research Institute, Singapore.

ABSTRACT

The corneal endothelium is a terminally differentiated tissue that is typically considered non-proliferative *in vivo*. Corneal endothelial dystrophies, including Fuchs' endothelial dystrophy (FED), are a significant cause of dysfunction, ultimately leading to corneal edema. Corneal transplantation is a well-established and effective treatment for corneal endothelial dysfunction. This condition is particularly prominent post-cataract surgery, which increases the risk of corneal transplant failure. However, the global shortage of human donor corneas has prompted ongoing research into alternative treatment approaches. Utilizing engineering solutions to model Fuch's endothelial dystrophy and investigating the mechanical properties of Descemet's membrane (DM) are pivotal for advancing our understanding and improving treatment options.

This research had two aims to advance our understanding of FED. The first aim was to investigate how human corneal endothelial cells (HCEC-B4G12) respond to synthetic guttata (S-guttata) pillars, with a specific emphasis on cell apoptosis, gene expression, and cytoskeletal changes. Subsequent examination of B4G12 cell responses to these pillars revealed induction of early and late apoptosis, with significantly higher rates observed on 20×20×20 (20 μm diameter, 20 μm spacing, and 20 μm height) and 40×80×20 (40 μm diameter, 80 μm spacing 20 μm, and height) pillars compared to unpatterned tissue culture polystyrene (TCPS) controls, respectively. Flow cytometry analysis confirmed enhanced early apoptosis on day 2, particularly on the 20×20 ×20 pillars. The α1 type V collagen (Col5A1) coating, which was shown to be highly expressed on large guttata in FED patients' DM, on S-guttata enhanced the cell apoptosis level on the larger 40×80×20 pillars. Moreover, the results demonstrated cytoskeletal stress induction in B4G12 cells in contact with S-guttata pillars, as evidenced by the increased alpha smooth muscle actin (α-SMA) and phosphorylated-myosin light chain 2 (pMLCK) expression levels, suggesting a potential

mechanism underlying the observed apoptotic response. The RT-qPCR results revealed differential modulation of oxidative stress-related gene expression in B4G12 cells on S-guttata pillars, with upregulation of NQO1 and SOD2 on 40 μm pillars and downregulation of SOD2 on 20×20×20 pillars. The second aim was to characterize and develop a method to measure the mechanical properties of human DM across distinct regions, including the central (CE), peripheral (PE), and transition zone (TZ). Variations in the thickness were observed, with TZ being the thickest region, followed by CE and PE. Furthermore, the stiffness analysis revealed that the TZ exhibited the lowest stiffness compared to the CE and PE regions. Our developed approach can be used to noninvasively measure DM thickness, and these findings will contribute to advancing our knowledge of corneal endothelial dystrophy and have the potential to improve current therapies, ultimately benefiting clinical outcomes and patient well-being.

ACKNOWLEDGEMENTS

I would like to extend my heartfelt gratitude to Professor Evelyn KF Yim, my supervisor, for her unwavering guidance and continuous support throughout my research. Her expertise and encouragement have played a pivotal role in during my study at University of Waterloo. I am particularly grateful for the opportunity to learn and grow under her guidance, especially during these uncertain times.

I would like to acknowledge our past lab members Deepak Jain and Wesley Luu for their contributions to the preliminary data for aim 1 and aim 2. This includes their work on immunostainings (Annexin V and PI, TUNEL assay, and α-SMA), as well as their efforts in measuring human Desecemet's Membrane stiffness.

I would like to acknowledge our collaborators Professor Jodhbir S Mehta and Dr. Gary S. L. Peh, along with their research group at Singapore Eye Research Institute for providing Desecemet's Membrane tissue samples and for their invaluable scientific discussions throughout the course of my research.

I would like to thank all my fellow lab members: Ms. Noura Ezzo, Ms. Abigail Conner, Mrs. Dency David, Mr. Fancheng Sun, Mr. Joshua Kunihiro, Ms. Olivia Graham, Mr. Fong Chenananporn and Dr. Yuan Yao. You have all been a pleasure to work alongside. Your help and friendship have made the many hours I spent in the lab more enjoyable. I wish you all the best in all your endeavors.

Additionally, I would like to acknowledge Professor Maud Gorbet (System Design Engineering, University of Waterloo) for her guidance in utilizing the flow cytometry machine.

I would also like to acknowledge Dr. Vivian Choh (School of Optometry and Vision Science, University of Waterloo) and Ms. Jessica Miller (Department of Biology, University of Waterloo) for their guidance and providing access to the cryostat.

I would also like to express my appreciation to my thesis committee members, Professor Maud Gorbet and Professor Tizazu Mekonnen, for providing valuable constructive criticism regarding the content of this thesis.

Lastly, I would like to thank my parents and my younger sister, Enkhbat Tundev, Munkhjargal Dugarjav and Enkhjargal Enkhbat for your tireless support. In times of joy, hardship, and everything in between, you have always been there for me. I could not have done this without you!

TABLE OF CONTENTS

AUTHOR'S DECLARATION ii

STATEMENT OF CONTRIBUTIONS iii

ABSTRACT iv

ACKNOWLEDGEMENTS vi

LIST OF FIGURES xi

LIST OF TABLES xiii

LIST OF ILLUSTRATIONS xiv

Chapter. 1 Introduction and Literature Review 1

1.1 Introduction and research background 1

1.1.1 Anatomy of the Cornea 1

1.1.2 Corneal endothelial dystrophy (CED) 3

1.2 Literature review 4

1.2.1 Introductions of DM and CE stem cell like population 4

1.2.2 Fuchs endothelial dystrophy (FED) 8

1.2.3 Current treatments and limitations 9

1.2.4 Models to study FED 10

Chapter. 2 Aims and Hypothesis 13

Chapter. 3 Corneal Endothelial Cells Response to S-guttata Pillars 15

3.1 Introduction 15

3.2 Materials and Methods 16

3.2.1 Fabrication of Polystyrene S-guttata Pillars 16

3.2.2 Optical Profilometry of the S-guttata Pillars 17

3.2.3 HCEC-B4G12 Cell Culture and Cell Seeding on S-guttata Pillars 17

3.2.4 Coating of S-guttata Pillars with α 1 type V collagen Human Recombinant Protein 18

3.2.5 Immunofluorescence Staining and Imaging 19

3.2.6 Terminal deoxynucleotidyl transferase dUTP nick end labeling (TUNEL) Assay ... 20

3.2.7 Flow Cytometry 20
3.2.8 Oxidative Stress Induced by Chemicals 21
3.2.9 RNA Extraction and Quantitative Reverse Transcription Polymerase Chain Reaction (RT-qPCR) 21
3.2.10 Immunofluorescence Image Analysis 23
3.2.11 Statistical Analysis 23
3.3 Results 23
3.3.1 Fabrication and Characterization of Polystyrene S-guttata Pillars 23
3.3.2 S-guttata Pillars Induced Early Apoptosis 25
3.3.3 Col5A1 Coated S-guttata Pillars Induced Early Apoptosis 29
3.3.4 S-guttata Pillars Induced Late Apoptosis 30
3.3.5 Cytoskeletal Stress Induced by S-guttata Pillars 33
3.3.6 Oxidative Stress Gene Expression on S-guttata Pillars 36
3.4 Discussion and Conclusion 37
3.4.1 Corneal guttata and cell apoptosis 37
3.4.2 Corneal guttata and Cell contractility 39
3.4.3 Corneal guttata and oxidative stress 40
Chapter. 4 Mechanical Properties of Human Descemet's Membrane 42
4.1 Introduction 42
4.2 Materials and Methods 43
4.2.1 Human Descemet's Membrane (DM) 43
4.2.2 LEXT film thickness measurement 44
4.2.3 Cryosectioning and Toluidine Blue Staining 45
4.2.4 Tensile Testing 45
4.2.5 Statistical Analysis 47
4.3 Results 47
4.3.1 Thickness of Human Descemet's Membrane 47
4.3.2 Stiffness of Human Descemet's Membrane 50
4.3.3 Suggested Protocol for non-destructive measuring DM thickness 51

4.4 Discussion and Conclusion **53**
4.4.1 Non-invasive approaches for film thickness measurement 53
4.4.2 Novel method to measure DM thickness with estimated RI 54
Chapter. 5 General Conclusions **55**
5.1 S-guttata pillars induced cell apoptosis **55**
5.2 Mechanical properties of human Descemet's membrane **55**
Chapter. 6 Future Works **57**
6.1 In Vitro Modelling of Fuchs Endothelial Dystrophy **57**
6.2 Characterization of Mechanical Property of Human Descemet's Membrane **57**
LETTER OF COPYRIGHT PERMISSION **59**
REFERENCES **65**
APPENDIX **73**

LIST OF FIGURES

Figure 1. The human cornea anatomy. 2

Figure 2. Scanning electron microscopy image of the peripheral cornea. 5

Figure 3. The expression of stem cell markers in human transition zone (TZ), peripheral endothelium (PE) and trabecular meshwork (TM) 7

Figure 4. B4G12 cell monolayer formation on polystyrene (PS) synthetic-guttata pillars. 9

Figure 5. Reflected confocal laser scanning microscope images of different S-guttatas and UP. 25

Figure 6. Immunofluorescence staining of early apoptotic cells on S-guttata pillars using Annexin V and propidium iodide (PI) with high cell density. 27

Figure 7. Assessment of S-guttata pillars induced apoptosis on S-guttata pillars using Annexin V and propidium iodide (PI) staining by flow cytometry with high cell density. 28

Figure 8. Immunofluorescence staining of early apoptotic cells on S-guttata pillars using Annexin V and propidium iodide (PI) with low cell density. 29

Figure 9. Immunofluorescence staining of early apoptotic cells on Col5A1 coated S-guttata pillars using Annexin V and propidium iodide (PI) with high cell density. 30

Figure 10. Detection of DNA fragmentation on S-guttata pillars using Terminal deoxynucleotidyl transferase-mediated dUTP nick end labeling (TUNEL) assay. 32

Figure 11. Quantification of TUNEL-positive cells on S-guttata pillars and pillars touching TUNEL-positive cells. 33

Figure 12. Cell contractility on S-guttata pillars 34

Figure 13. Phospho-Myosin Light Chain 2 (pMLCK) expression on S-guttata pillars 35

Figure 14. Relative mRNA expression of NQO1, SOD1 and SOD2 genes on S-guttata following two days. 37

Figure 15. LEXT film thickness measurement of representative DM in CE, PE and TZ regions. 49

Figure 16. Mechanical property of DM in various regions including Central (CE), Periphery (PE), Transition zone (TZ). 50

Figure 17. DM stiffness in various regions. 51

Figure A1. Assessment of S-guttata induced apoptosis using Annexin V and propidium iodide (PI) staining by flow cytometry after one day with high cell density. 73

Figure A2. Assessment of S-guttata induced apoptosis using Annexin V and propidium iodide (PI) staining by flow cytometry after two days with high cell density. 74

Figure A3. Brightfield imaging of representative DM CE, PE and TZ regions for gender comparison. 75

Figure A4. Relative mRNA expression of NQO1, SOD1 and SOD2 genes on TCPS and UP with menadione and tert-Butyl hydroperoxide following two days for titration assay. 76

Figure A5. Representative Strain-stress curve of human DM. 77

LIST OF TABLES

Table 1. Dimensions of S-guttata micro-structures used for studying cell apoptosis 17

Table 2. Media used for B4G12 cells 18

Table 3. Primary antibodies used for immunofluorescence staining 20

Table 4. Primer sequences for RT-qPCR 22

Table 5. Profile measurement of S-guttata pillars micro-structures used for studying cell apoptosis 25

Table 6. Human Descemet's Membrane sample information. 44

Table 7. Expected force resolutions and recommended maximum forces 46

Table 8. DM thickness and estimated RI 48

LIST OF ILLUSTRATIONS

Scheme 1. Experimental design of the study. 24

Scheme 2. Illustration of 3-point bend test. 47

Chapter. 1 Introduction and Literature Review

1.1 Introduction and research background

1.1.1 Anatomy of the Cornea

The cornea is a transparent and avascular tissue located at the most outer layer of the eye. It consists of five distinct layers including (I) epithelium; (II) Bowman's membrane; (III) stroma; (IV) Descemet's membrane (DM); (V) endothelium (**Figure 1**) [1]. Thickness of the human cornea in the central region is approximately 500 μm thick in healthy adults [2]. In the cornea, the nonkeratinized and stratified epithelium layer constitutes approximately 10% of tissue which has 4 to 6 cell layers 40-50 μm thick. The function of corneal epithelial cells is to ensure the integrity of the tear film-cornea interface by creating a barrier to the outside environment. It is vital to the refractive power of the eye and the prevention of toxins and microbes from entering the inner layers of the cornea. Bowman's layer lies just under the epithelium and this smooth layer is approximately 15 μm thick and assists the cornea to sustain its shape [3]. The bulk of the cornea is the corneal stroma, that roughly comprises 80-85% of the corneal and is approximately 450 μm thick. Keratocytes are the main cell type of the stroma, and it maintains the extracellular matrix (ECM) environment of stroma and corneal transparency. The DM is located at the posterior boundary of the stroma, and secretion from the CECs after birth can contribute up to an additional 10 μm in thickness with age [4]. The corneal endothelium (CE), located at the posterior of the cornea, forms a monolayer of hexagonal cells.

The human corneal endothelium (CE) is essential for the regulation of corneal hydration, maintaining the appropriate thickness of the cornea, and keeping it transparent [5]. Substantial loss of the human corneal endothelial cell (HCECs) affects corneal deturgescence (state of relative dehydration necessary to maintain the transparency of the cornea of the eye), resulting in increased

stromal thickness, loss of visual acuity, and when left untreated, will lead to corneal blindness. Within the human eye, HCECs are principally non-proliferative, mitotically inactive and arrested at the G1 phase of cell cycle [6, 7], but retain the capacity to proliferate *in vitro* [8, 9].

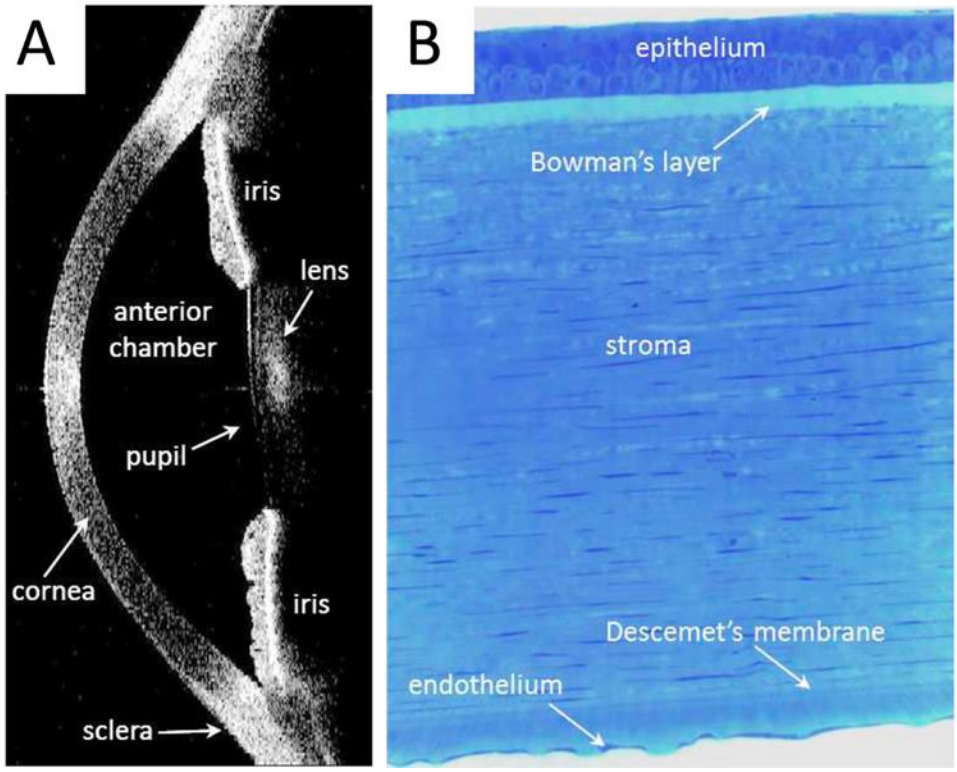


Figure 1. The human cornea anatomy.
(A) *In vivo* cross-section of the cornea and anterior eye by anterior segment optical coherence tomography. The bright areas indicate light scatter while the dark areas are transparent. The bright area in the central cornea is an artifact. (B) Histologic view of the human cornea with toluidine blue staining, indicating the five principal layers of the normal cornea. Copyright 2013 Neil Lagali. Originally published in [10] under Creative Commons Attribution 3.0 Unported license. Available from DOI: 10.5772/55216.

Basement membranes are specialized ECM structures that vary by organ and exhibit a high degree of organization [11]. Descemet's membrane (DM) is a vital component of the cornea, playing a crucial role in maintaining its structure, transparency, and overall health. In DM, there is a composition of both collagenous and non-collagenous elements, which notably include the four primary components, namely laminins, collagen type IV, nidogens (known as entactins), and

perlecan (known as basement membrane-specific heparan sulfate proteoglycan core protein). These constituents are commonly found in the majority, if not all, basement membranes [11, 12]. This membrane serves a dual purpose: it anchors the corneal endothelium to the cornea while permitting the passage of essential nutrients and large molecules into the corneal stroma. Its role in adhering to the single layer of corneal endothelial cells significantly contributes to the integrity of the cornea, which is essential for regulating hydration and ensuring optical clarity [11, 13].

1.1.2 Corneal endothelial dystrophy (CED)

Corneal endothelial dystrophies encompass conditions such as Fuchs' Endothelial Dystrophy (FED), Posterior Polymorphous Dystrophy (PPCD), and congenital hereditary endothelial dystrophy (CHED). Of these, FED is the most common among corneal endothelial dystrophies, typically manifesting between the ages of the fourth and fifth decades of life [14]. In the case of FED, there is a gradual decline in the CE, leading to the thickening of the DM and the development of distinct ECM deposits known as guttata. Individuals with FED often suffer from glare and reduced vision due to light scattering caused by these corneal guttata and corneal swelling. In the case of PPCD, the CE cells undergo a transformation, taking on a phenotype that closely resembles that of epithelial cells. This transformation results in distinct clinical characteristics, including the presence of opacities, vesicular lesions, and ‘track-like’ patterns resembling tracks across the corneal endothelium [15]. CHED is an autosomal recessive disorder associated with genetic mutations in SLC4A11, a gene responsible for encoding a transmembrane bicarbonate transporter [16].

Fuchs’ endothelial dystrophy (FED) is a condition affecting the cornea, primarily stemming from the degeneration of the corneal endothelium. It is characterized by the gradual loss of CECs, alterations in the hexagonal pattern of these cells, and the simultaneous development of deposits

known as guttata or guttata within the ECM [17]. When the density of CECs significantly lower, the cornea experiences edema, which results in vision loss [18]. In most instances, FED is a condition that advances slowly with age, affecting around 4% of the population aged 40 and older [19]. Studies have indicated that common final pathways play a role in endothelial cell death in FED [20, 21]. Specifically, a compromised antioxidant defense mechanism makes the corneal endothelium vulnerable to oxidative stress. This oxidative stress, in turn, leads to damage to nuclear and mitochondrial DNA, causing mitochondrial dysfunction [20]. Abnormal deposition of ECM is associated with TGFBI-mediated endoplasmic reticulum (ER) stress, leading to the activation of the unfolded protein response (UPR). Consequently, this exacerbates mitochondrial dysfunction and triggers the corneal endothelial cells apoptosis [22-25].

Apoptotic cell death has been shown in FED, as indicated by terminal deoxynucleotidyl transferase dUTP nick end labelling (TUNEL) and DNA fragmentation assays [26]. A significant catalyst for apoptosis is the presence of macromolecular damage, such as that to DNA, resulting from oxidative stress. The corneal endothelium is unique in that it is in a post-mitotic state, meaning it does not undergo cell division, making its genetic material particularly susceptible to apoptosis triggered by reactive oxygen species (ROS). Jurkunas *et al.* observed notably higher levels of oxidative DNA damage in corneal endothelial cells affected by FED when compared to those in normal, age-matched control groups [20].

1.2 Literature review

1.2.1 Introductions of DM and CE stem cell like population

A distinctive subgroup of cells known as 'Schwalbe's line cells' was first documented in 1982 [27]. However, a conclusive endothelial stem cell has not been pinpointed. These cells were situated at the peripheral corneal border within the anterior trabecular meshwork, as described by

Raviola [27]. Subsequent research has revealed that cells within this corneal region exhibit ongoing cell division activity and display the presence of stem cell markers, including telomerase, alkaline phosphatase, HNK-1, p75 neurotropin receptor, and nestin [28-30]. Recently, Yam *et al*. comprehensively examined this outer segment of the cornea through ultrastructural analysis, using advanced techniques like serial block face-scanning electron microscopy and three-dimensional reconstruction [31]. The authors demonstrated that within the peripheral cornea's 'transition zone' immunohistochemical analysis allowed for the distinction of two discrete regions, namely the inner and outer zones (**Figure 2**). An inner transition zone (TZ) enriched with progenitor cells expressing stem/progenitor markers such as Sox2, CD34, Lgr5, and TERT. These progenitor-like cells were localized on the inner TZ surface and the underlying stroma. Notably, Lgr5-positive cells formed digitated clusters extending from the inner TZ to the peripheral endothelium (PE). These findings suggest potential regenerative capacity for the corneal endothelium.

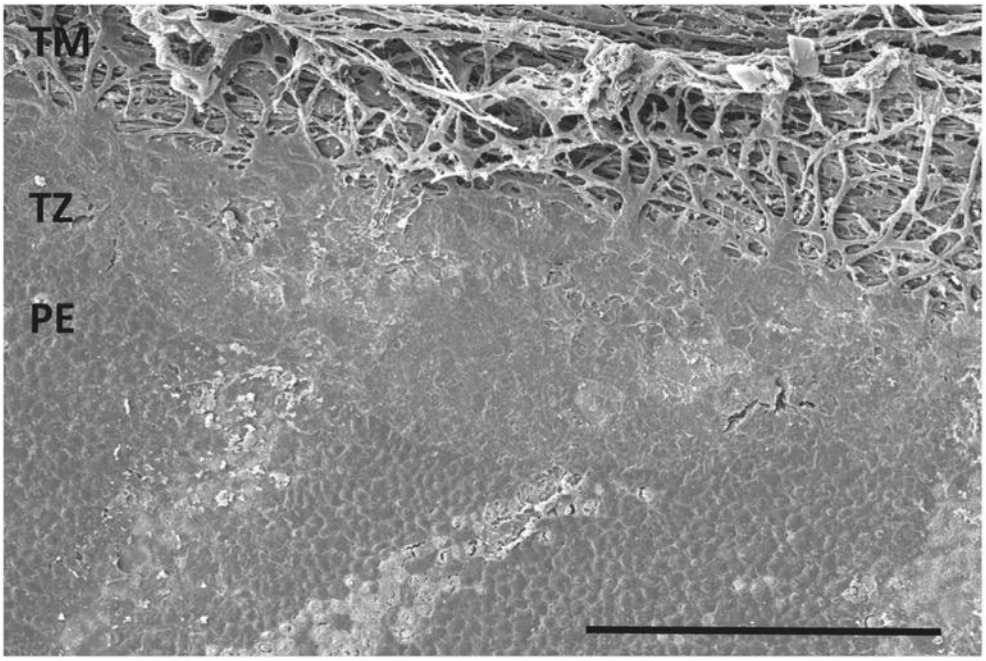


Figure 2. Scanning electron microscopy image of the peripheral cornea.
The endothelial progenitors are located in the transition zone (TZ) between the peripheral endothelium (PE) and the trabecular meshwork (TM). Scale bar is 300 μm. Copyright 2013 Gary

Hin-Fai Yam. Originally published in [31] under Creative Commons Attribution 4.0 Unported license. Available from DOI: 10.3390/cells8101244.

The primary approach for addressing CED involves corneal transplantation, which entails replacing the impaired cornea with a healthy one from a donor. While corneal surgery has seen notable progress in recent years, several challenges persist. These challenges encompass the availability of donor tissue, the limited longevity of transplants, prolonged reliance on immunosuppressive medications, and the requirement for specialized surgical skills [32, 33]. Yam *et al.*, identified cells with stem-like characteristics in the stromal area within the inner transition zone (TZ), characterized by a significant ratio of nucleus size to cytoplasm size [31]. These findings suggest that the inner TZ may serve as a region enriched with potential CE progenitor cells (**Figure 3**). Thus, conducting further research to understand the differentiation and promotion of migration of human CE stem cell-like cells into a functional corneal endothelium holds promise for the translational application of corneal endothelial regenerative therapy.

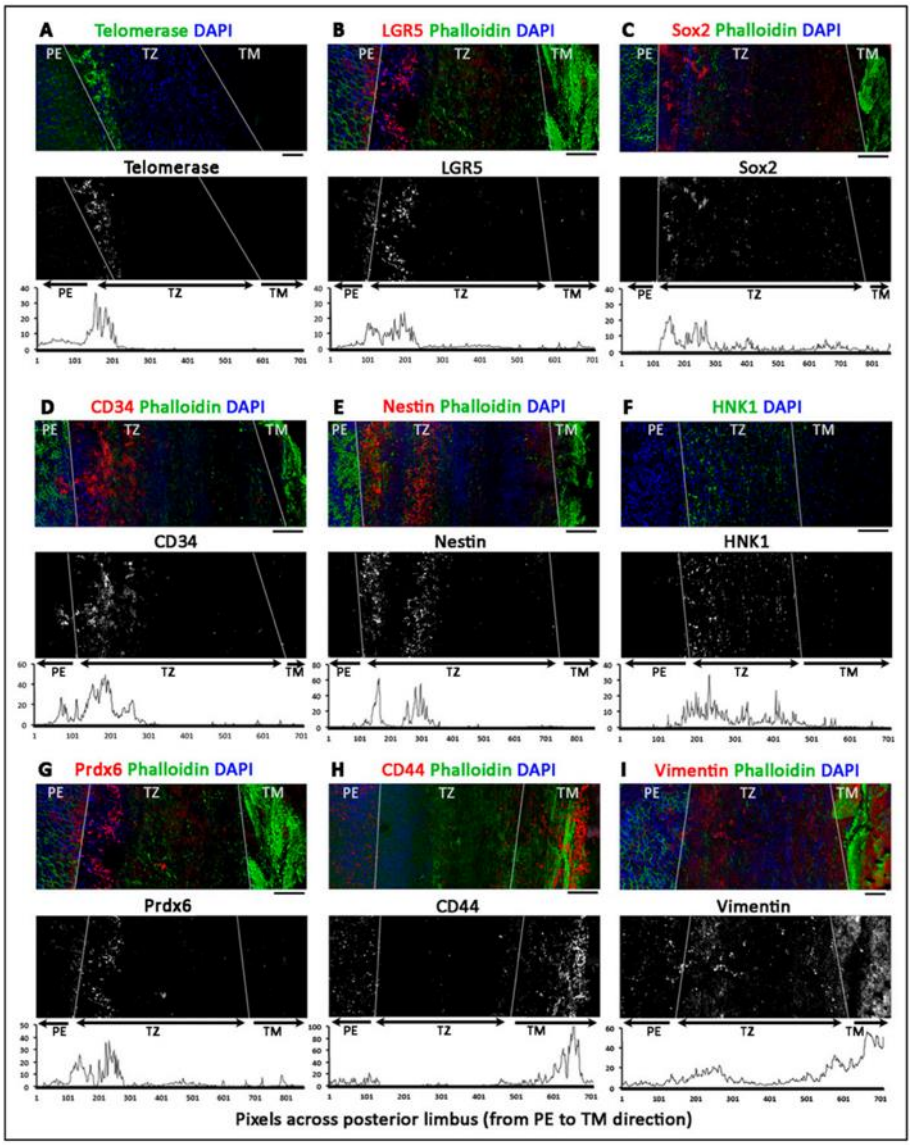


Figure 3. The expression of stem cell markers in human transition zone (TZ), peripheral endothelium (PE) and trabecular meshwork (TM)

The expression of (A) telomerase (TERT), (B) Lgr5, (C) Sox2, (D) CD34, (E) nestin and (G) Prdx6 were more expressed in the inner TZ. (F) HNK1 and (I) vimentin were detected in the entire TZ region. In contrast, outer TZ and TM had (H) CD44 and vimentin signal. White lines delineate borders between TM, TZ and PE. The top images represent the original-colored confocal pictures, the middle grey-scaled images are single antibody-specific channel after threshold adjustment and the bottom graphs are the signal intensity profiles from PE across TZ to TM (x-axis represents distance in pixels and y-axis is the relative intensity levels). Scale bars: 50 μm. Copyright 2013 Gary Hin-Fai Yam. Originally published in [31] under Creative Commons Attribution 4.0 Unported license. Available from DOI: 10.3390/cells8101244.

1.2.2 Fuchs endothelial dystrophy (FED)

FED is a condition characterized by dysfunctional CE and the accumulation of non-banded collagen, known as guttata, on the DM due to abnormal ECM deposition. CECs are arrested in the G1 phase of the cell cycle, rendering them unable to proliferate to repair damage. This renders the endothelium highly delicate and prone to failure as a result of disease or injury such as FED [6, 9]. The prevalence of FED varies among different regions, genders, and ethnic groups [34, 35]. It stands as one of the most common genetic disorders affecting the CE [36, 37]. According to data from the Eye Bank Association of America's 2016 Statistical Report, more than 28,000 corneal transplant surgeries were conducted in the United States because of corneal edema associated with FED, establishing it as a leading reason for such procedures [38].

The abnormal ECM secretion results in the formation of guttata, which is a significant feature in FED, causing impairment in vision. The effect on cellular function depends on the existence of guttata, determined by their dimensions and density. Cell apoptosis evidently plays vital role in the degeneration of the corneal endothelium [26, 39, 40]. The accumulation of oxidative DNA damage results in the loss of endothelial cells around the bases of guttata, dysfunction of mitochondria, and degeneration of ocular tissue [41, 42]. In 2016, Rizwan *et al.* developed synthetic guttata-like microstructures known as S-guttata pillars [43] to study the formation of HCEC monolayer in microenvironment that mimics FED (**Figure 4**). They found that S-guttata pillars with 20 μm diameters, spacing, and height, as well as 40 μm diameters, could disrupt primary CEC monolayer formation. However, the precise mechanism underlying the apoptosis of CECs during FED remains elusive.

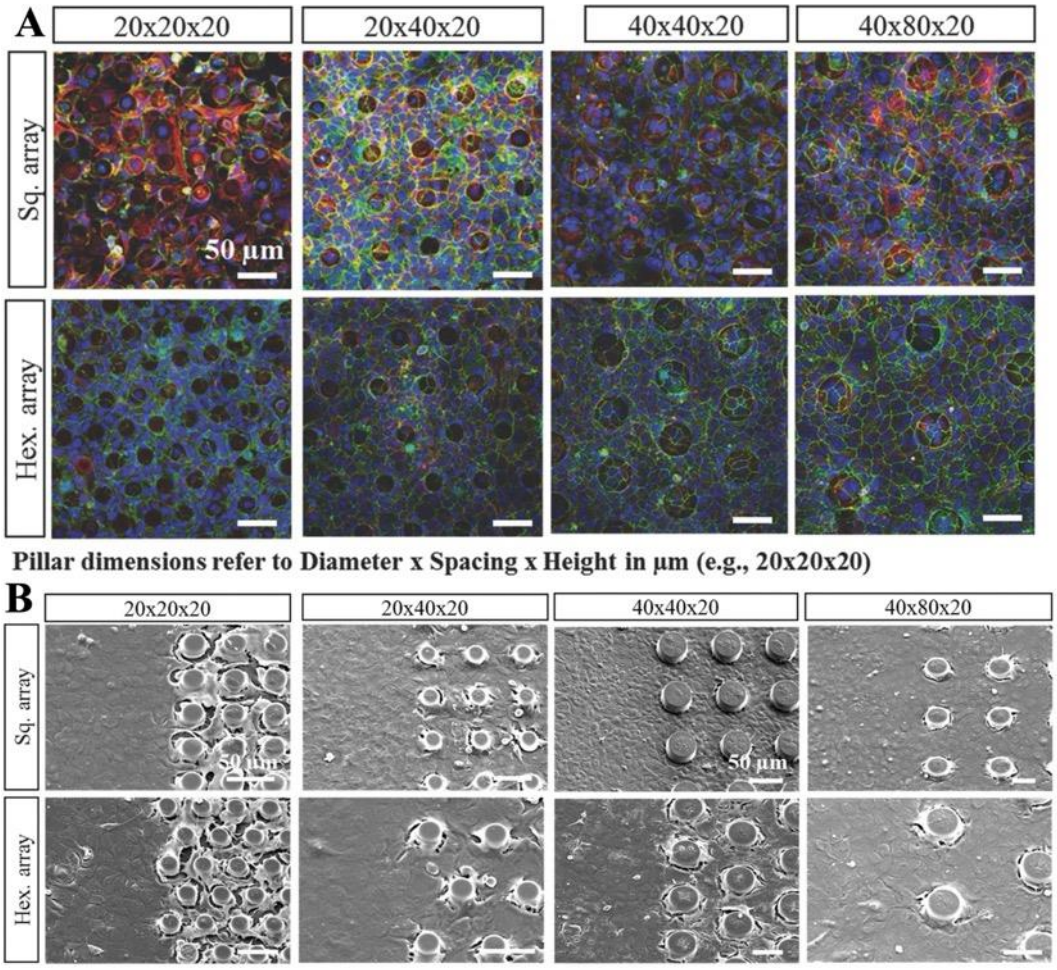


Figure 4. B4G12 cell monolayer formation on polystyrene (PS) synthetic-guttata pillars. (A) B4G12 cell monolayer formation of migrated B4G12 cells on various s-guttata pillars. (B) SEM characterization of the interaction of B4G12 cells with s-guttata pillars. Comparison of B4G12 cell monolayer formation on s-guttata pillars of various spacing and diameter versus s-guttata-free area on polystyrene substrates. The images represent cell monolayer formed after the cell migration, excluding the possibility of any cells on top of s-guttata microstructures during cell seeding. Adapted with Permission [43]. Copyright 2016, Wiley-VCH.

1.2.3 Current treatments and limitations

In 1998, Melles *et al.* described selective endothelial replacement surgery for the first time. Since then, significant advancements in the procedure have led to DSAEK and Descemet Membrane Endothelial Keratoplasty, which have greatly enhanced visual results [33]. Corneal transplantation is the established and most effective treatment for addressing corneal endothelial dysfunction [33, 44]. In the field of corneal transplantation, the shortage of suitable donor corneas

poses a significant challenge on a global scale. Particularly, considering that corneal transplantation is a one-to-one surgery where one donor cornea is required for each recipient [45]. The progress in selectively replacing the damaged corneal endothelium has raised the bar in terms of safety and effectiveness. There are several non-surgical treatment options including topical administration of antibiotics, steroids, nonsteroidal anti-inflammatory drugs to relieve symptoms [46-48]. However, only a corneal transplantation is the definitive treatment to reverse corneal blindness for corneal endothelium diseases such as end-stage FED. Full-thickness corneal transplantation or penetrating keratoplasty (PK) where the whole corneal button is transplanted is being gradually replaced with endothelial keratoplasty (EK), which has gained widespread acceptance as the established standard treatment approach [14, 33]. Nevertheless, the global shortage of human donor corneas has led to extensive research into alternative therapies.

1.2.4 Models to study FED

Model development for studying FED encompasses various approaches, ranging from molecular mechanisms to the microenvironment. Given the diverse understanding of FED etiology, several disease models have been established, each serving distinct purposes. Animal models, including mice [49, 50], rabbits [51, 52], feline [53, 54] and monkeys [55, 56], offer opportunities to study disease mechanisms and test potential therapies. Cell culture models (*in vitro models*), including primary [43, 54, 57] and immortalized human corneal endothelial cells [58-60] and induced pluripotent stem cells (iPSCs) [61], provide platforms for understanding cellular and molecular aspects of FED. *Ex vivo* human corneal tissues have been extensively used to study oxidative stress, cell apoptosis, cell migration, and surgical procedures in FED [42, 62-64]. *In vivo* imaging models, such as corneal confocal microscopy [65] and optical coherence tomography (OCT) [66], facilitate longitudinal monitoring of disease progression in patients.

In vitro models play a crucial role in understanding FED pathogenesis and exploring potential therapeutic interventions. Tissue-engineered cornea models, developed since the late 20th century, offer a platform for investigating drug responses, wound healing, and reducing reliance on animal models [67]. These models aim to replicate the complex microenvironment of the cornea, providing insights into disease mechanisms and treatment strategies.

Primary CECs isolated from FED patients serve as valuable tools for studying cell behavior and disease progression. Despite challenges in maintaining their characteristic morphology and preventing endothelial-to-mesenchymal transition (EndMT), advancements such as dual media culture systems have shown promise in addressing these obstacles [67]. Studies have demonstrated the successful cultivation of CECs from FED patients, revealing insights into cell expansion, morphology, and potential predictors of successful culture establishment [68]. Furthermore, the phenomenon of "phenotypical switch" observed in primary FED cells cultured *in vitro* underscores the influence of the culture environment on cellular behavior [68, 69]. Despite initial challenges, the isolation and expansion of viable FED cells offer opportunities to explore cell apoptosis mechanisms and therapeutic targets.

Immortalized CEC lines, such as those induced by SV40 large T-antigen or human Telomerase Reverse Transcriptase (hTERT), provide alternative models for studying FED [58, 70]. These immortalized lines offer advantages in terms of accessibility and reproducibility, bypassing challenges associated with primary cell culture [58, 59]. However, concerns remain regarding their altered behavior and responses, necessitating careful interpretation of experimental findings [58-60]. Despite limitations, immortalized CEC lines have contributed valuable insights into modelling FED. For instance, studies utilizing SV40-immortalized CECs have revealed oxidative imbalance and increased oxidative DNA damage in FED corneal endothelium, highlighting potential

molecular targets for intervention [20]. Additionally, the establishment of immortalized FED cell lines has facilitated investigations into mitochondrial dysfunction and dysregulated cellular processes implicated in FED progression [71, 72].

Overall, the establishment and development of FED models represent essential steps toward unraveling the complexities of this disease and developing effective therapeutic strategies to improve patient outcomes.

Chapter. 2 Aims and Hypothesis

Corneal endothelial dystrophy can result in the loss of corneal endothelial cells (CECs), leading to corneal edema (swelling) and eventual corneal blindness. Since human CECs do not possess proliferative capabilities *in vivo*, thus the regenerative potential is limited in corneal endothelium. As opposed to the potential regeneration with limbal stem cells for the epithelial layer, the regeneration capacity for CED is constrained. Corneal transplantation is the primary treatment, but the treatment option is hindered by donor scarcity. In this study, my aim is to engineer solutions to better comprehend the challenges posed by CED and develop novel treatment approaches.

By creating engineering solutions to address the complexities of endothelial dystrophy, we can pave the way for improved treatments. Formulating two sub-hypotheses, our objectives aim to enhance our understanding of CED and unravel the regenerative potential of the corneal endothelium.

Aim 1: Investigate CECs Responses to S-guttata pillars: To systematically investigate and characterize the cellular responses of CECs (HCEC-B4G12) to S-guttata pillars, focusing on cell apoptosis, changes in gene expression and cytoskeletal tension.

Hypothesis 1: S-guttata pillars interacts with HCEC-B4G12 cells triggering specific cellular responses that contribute to the apoptotic cascade observed in FED. These cellular responses are expected to be contingent on specific features of S-guttata pillars and concurrent alterations in cytoskeletal tension within HCEC-B4G12 cells. Specifically, the increased cytoskeletal tension induced by S-guttata pillars plays a pivotal role in initiating and advancing apoptosis.

Aim 2: Characterize Properties of Human Descemet's Membrane: To characterize the stiffness and thickness of Descemet's Membrane in various regions using non-destructive approach.

Hypothesis 2: The stiffness and thickness of DM will vary between the different regions.

Chapter. 3 Corneal Endothelial Cells Response to S-guttata Pillars

3.1 Introduction

Corneal diseases are the third leading cause of blindness. The causes of corneal blindness include congenital or acquired through injury, trauma, infection, or surgical operation in the eye, resulting in the loss of transparency or visual dysfunctions [73, 74]. The inability for the human corneal endothelial cells (HCECs) to replace damaged or lost cells *in vivo* is a significant factor in the development of human corneal endothelial diseases [75]. Guttata, which are small excrescences found on the DM of the cornea, is most pronounced in the central corneal region and reduces gradually towards the periphery [76]. These guttata lesions resemble convex microdome-like or micropillar-like structures, varying in terms of diameter, height, and spacing which depend on the stage of FED advancement.

Investigating CECs responses to environmental factors is important for elucidating the pathophysiology of corneal endothelial diseases such as FED and developing effective treatments [20]. The CE is essential for maintaining corneal transparency and hydration balance, and dysfunction or loss of CECs can lead to corneal edema and vision impairment [5]. Environmental factors such as oxidative stress [20] and mechanical stress [77] can impact CECs function and viability, highlighting the need to study their responses to these stimuli. By understanding how CECs respond to biophysical cues, particularly from guttata, researchers can identify potential therapeutic strategies to protect and regenerate the corneal endothelium [78-81], ultimately improving patient outcomes in various corneal diseases.

A clinical indication and characteristic of FED is the existence of distinct abnormal collagen secretion, termed corneal guttata, situated on the DM on the inner surface of the cornea [40, 82, 83]. The guttata emerge centrally on the DM during the disease's initiation. As the guttata become

larger, they reduce the cell cytoplasm on the apical side of the endothelium, resulting in cell death and progressive deterioration of endothelial function [84]. The density of guttata is highest at the central region of the cornea and gradually reduces towards the periphery. Additionally, depending on the stage or progression of FED, guttata can vary widely in terms of diameter, spacing, and height [76]. Previous investigations using transmission electron microscopy (TEM) have described guttata lesions as resembling convex microdome or micropillar structures, exhibiting various diameters, heights, and spacing, contingent upon the stage of FED advancement [84].

Guttata, often associated with inducing cell apoptosis, are a key factor contributing to the degeneration of corneal endothelial cells in FED patients [26, 40]. These abnormal structures are characterized by abnormal collagen deposition [83, 85] and are secreted by dysfunctional corneal endothelial cells, potentially as a result of aging. Notably, various types of collagens, including type I, II, III, IV, V, and VIII, are substantially presented in human corneal guttatas [86, 87].

In this chapter, we aim to investigate the effect of S-guttata pillars with various dimensions on B4G12 cell apoptosis and cell behavior. Previously, we have developed a S-guttata pillars using soft lithography and hot embossing approach [43]. We have also investigated the effect of α1 type V collagen (Col5A1) on cell apoptosis in S-guttata pillars to explore potential differences in apoptotic induction between the topographical features of guttata and protein composition. Furthermore, we aim to develop a better understanding of the FED by recapitulating the disease microenvironment.

3.2 Materials and Methods

3.2.1 Fabrication of Polystyrene S-guttata Pillars

Polydimethylsiloxane (PDMS) microwells were utilized as stamps to fabricate S-guttata pillars using the hot embossing technique, as described previously [88]. Briefly, polystyrene (PS)

samples underwent a heat embossing process at 220°C for 90 seconds under 5 bar pressure. Subsequently, they were cooled at room temperature for 45 seconds, still under 5 bar pressure. For unpatterned (UP) control samples, PS samples were embossed with a plain PDMS master without any topography. Six different dimensions of S-guttata pillars were selected for cell apoptosis (**Table 1**). Before being used as cell culture substrates, all PS samples were thoroughly cleaned with absolute ethanol, dried, and subjected to plasma treatment for 60 seconds at 60W with air (Zepto, Diener, Germany). The samples were then sterilized using 70% ethanol for 10 minutes and exposed to UV irradiation for 30 minutes. Subsequently, the samples were rinsed once with sterile filtered 1X Phosphate-buffered saline (PBS) and directly seeded with cells.

Table 1. Dimensions of S-guttata micro-structures used for studying cell apoptosis

Diameter (μm)	Spacing (μm)	Height (μm)	Referred to as
20	20	20	20x20x20
20	40	20	20x40x20
40	40	20	40x40x20
40	80	20	40x80x20
20	20	10	20x20x10
40	80	10	40x80x10

3.2.2 Optical Profilometry of the S-guttata Pillars

Optical profilometry was performed using the LEXT OLS5000 3D Laser Scanning Microscope (Olympus, Tokyo, Japan). After the hot embossing process, surface topography profiles were generated for each sample. The top view of all samples was captured using the LEXT OLS5000 3D Laser Scanning Microscope.

3.2.3 HCEC-B4G12 Cell Culture and Cell Seeding on S-guttata Pillars

HCEC-B4G12 (B4G12) cells were purchased from DSMZ (Braunschweig, Germany). B4G12 cells were maintained in regular media composed of 10% fetal bovine serum (FBS) (Wisent, Saint-Jean-Baptiste, Quebec, Canada) and 1% penicillin–streptomycin (Gibco, Carlsbad, California, USA) in DMEM (10-017-CV, Corning, New York City, NY, USA). Serum-free media composed of DMEM, 1% penicillin–streptomycin and basic fibroblast growth factor (bFGF) (Invitrogen, Massachusetts, USA) was used for Col5A1 coated S-guttata induced apoptosis experiment (**Table 2**). B4G12 cells were seeded at a density of 3000 cells/mm² and 1000 cells/mm² directly on top of S-guttata. The cells were then cultured for 1 day and 2 days, respectively, incubated at 37° C and 5% CO_2.

Table 2. Media used for B4G12 cells

	Volume/50 ml media (Final Concentration)	
	Regular media	Serum-free media
DMEM high glucose	45 ml	50 ml
Fetal bovine serum	5 ml	-
Penicillin/streptomycin (100X)	0.5 ml (1X)	0.5 ml (1X)
bFGF	-	10 ng/ml^{-1}

3.2.4 Coating of S-guttata Pillars with α 1 type V collagen Human Recombinant Protein

S-guttata pillars underwent coating with α1 type V collagen (Col5A1) human recombinant protein (Abnova Taiwan Corporation, Taipei, Taiwan) at a density of 5 μg/cm² for 1 hour at room temperature prior to cell seeding. Before applying the Col5A1 human recombinant protein, S-guttatas were initially coated with FNC Coating Mix® (serum-free tissue culture reagent containing fibronectin, collagen and albumin) (Athenaes, Baltimore, USA) to enhance cell attachment.

3.2.5 Immunofluorescence Staining and Imaging

After 1 day and 2 days of cell culture, the cell media was removed from the samples, and the cells were washed two times with 1X PBS. The samples were then incubated in the dark for 15 minutes with 100 µL of Annexin V conjugates and propidium iodide (PI) solution in Annexin V binding buffer (composed of 10 mM HEPES, 140 mM NaCl, and 2.5 mM $CaCl_2$ in PBS, pH 7.4). The Annexin V and PI solution contained 25 µL of Annexin V dye (A13201, Thermo Fisher Scientific, USA) and 2.5 µL of PI dye (100 µg/ml, P1304MP, Thermo Fisher Scientific, USA).

Following the incubation, the cells were washed twice with annexin binding buffer and then fixed with 4% paraformaldehyde (PFA) in annexin binding buffer. Subsequently, the cells were washed twice with annexin binding buffer and counterstained with 4',6'-Diamidino-2-Phenylindole, Dihydrochloride (DAPI) solution (1:1000) (D9542, Sigma Aldrich, USA) for 15 minutes at room temperature. After the staining, the cells were mounted on glass coverslips for analysis under a fluorescence microscope (Axio Observer Z1, Zeiss GmBH).

For cytoskeletal markers, B4G12 cells on S-guttata pillars at day 2 were fixed with 4% PFA and permeabilized with 0.1% Triton X-100 in 1X PBS. The cells were blocked with 10% goat serum and 1% bovine serum albumin (BSA) in 1X PBS overnight at 4 °C. Alpha smooth muscle actin (α-SMA) and phosphorylated-Myosin Light Chain 2 (pMLCK) was labeled overnight at 4 °C with mouse (α-SMA) and rabbit (pMLCK) monoclonal primary antibody diluted at 1:50 and 1:75 in 1X PBS, respectively (**Table 3**). Samples were than washed twice for 5 min per washing cycle with a solution of 1% goat serum in 1X PBS. Subsequently, the samples were incubated for 1 h at room temperature with Alexa Fluor 488-conjugated goat anti-mouse IgG antibody (A11001, Thermo Fisher Scientific, USA) diluted at 1:750 in 1X PBS, separately. Nuclei were stained with DAPI at 1:1000 and cytoskeleton were stained with Phalloidin (A12379, Thermo Fisher Scientific,

USA) at 1:500 for 20 min at room temperature followed by washing. Then samples were mounted on glass cover slip with Fluoromount-G™ mounting medium (00-4958-02, Thermo Fisher Scientific, USA) and imaged using fluorescence microscope (Axio Observer Z1, Zeiss GmBH).

Table 3. Primary antibodies used for immunofluorescence staining

Name	Company	Catalog number	Host species	Dilution
α-Smooth muscle actin	Abcam	Ab7817	Mouse	1:50
Phospho-Myosin Light Chain 2 (Ser19)	Cell Signaling Technology	3671S	Rabbit	1:75

3.2.6 Terminal deoxynucleotidyl transferase dUTP nick end labeling (TUNEL) Assay

After 1 day and 2 days of cell culture, the B4G12 cells were fixed for immunofluorescence staining and imaging. Fixation was achieved using 4% paraformaldehyde, followed by permeabilization with 0.2% Triton X-100 (T8787, Sigma Aldrich) and blocking with 1% (w/v) bovine serum albumin or 10% (v/v) goat serum in 1X tris-buffered saline (TBS, Atlanta, GA, USA) (pH 7.4) (Bp2471-500 Fisher BioReagents).

For the late apoptosis analysis in B4G12 cells on S-guttata pillars, the DeadEnd™ Fluorometric TUNEL system (G3250, Promega, USA) was used following the manufacturer's instructions. Fluorescence signals were detected using a confocal microscope (Axio Observer Z1, Zeiss GmBH). The frequency of apoptotic cells in B4G12 cells was quantified by determining the percentage of TUNEL-positive cells in five random microscopic fields per specimen.

3.2.7 Flow Cytometry

After 1 day and 2 days of cell culture, the cells were washed with 1X PBS and harvested using TrypLE™ Express Enzyme (1X) with phenol red (12605010, Thermo Fisher Scientific, USA).

Subsequently, the cells were washed with ice-cold PBS and resuspended in Annexin binding buffer. Annexin V-FITC and PI were added to the cell suspension following the manufacturer's instructions, and the samples were then incubated for 15 minutes at room temperature in the dark. Flow cytometry analysis was performed thereafter.

For flow cytometry analysis, a total of 3000-6000 events were acquired for each sample after gating for single cells based on forward and side scatter properties using Becton Dickinson FACS Calibur flow cytometer (Mountain View, CA, USA). To validate the flow cytometry analysis, negative and positive controls were included. The negative control comprised untreated cells incubated with Annexin V-FITC and PI, while the positive control involved cells treated with 50% ethanol for 2 minutes. The negative control cells displayed minimal Annexin V-FITC and PI staining, confirming the absence of spontaneous apoptosis (≤ 4%). In contrast, the positive control cells showed a significant increase in both early apoptotic and dead populations, validating the sensitivity of the assay and the functionality of the staining procedure. Data analysis was performed using Floreada.io online software.

3.2.8 Oxidative Stress Induced by Chemicals

B4G12 cells were seeded on TCPS and unpatterned (UP) as a positive control, at a density of 3000 cells/mm². Subsequently, the cells were incubated at 37°C and 5% CO_2 for 3 hours in the presence of 250 µM tert-butyl hydroperoxide solution (tBHP) (458139, Sigma Aldrich, USA) and 33.5 µM menadione solution (MN) (M5625, Sigma Aldrich, USA) to induce oxidative stress. Prior to use these concentrations, a titration assay was conducted to identify the most effective concentration of each chemical for inducing oxidative stress in the cells.

3.2.9 RNA Extraction and Quantitative Reverse Transcription Polymerase Chain Reaction (RT-qPCR)

Total RNA was extracted using the QIAGEN RNeasy Mini Kit (74104, QIAGEN, Germany) following the manufacturer's instructions. The quality and quantity of the isolated total RNA samples were assess using the NanoDrop ND-1000 Spectrophotometer before proceeding with cDNA synthesis. The RNA was then reversely transcribed into cDNA using the iScript™ cDNA Synthesis Kit (170-8891, Bio-Rad, Hercules, CA, USA) according to the manufacturer's instructions. Subsequently, the cDNA samples were quantified using the NanoDrop ND-1000 Spectrophotometer and diluted in DPEC-treated RNase-free DI water.

RT-qPCR was performed using an Applied Biosystems Stoneless™ RT-qPCR system (Applied Biosystems, USA) to detect the relative expression levels of NAD(P)H quinone dehydrogenase 1 (NQO1), superoxide dismutase 1 (SOD1), and superoxide dismutase 2 (SOD2) genes (**Table 4**). The reaction conditions were set as follows: 40 cycles of pre-denaturation at 95°C for 2 minutes, denaturation at 90°C for 5 seconds, annealing and extension at 60°C for 30 seconds. The relative $2^{-\Delta\Delta Ct}$ method was used to calculate the relative expression of NQO1, SOD1, and SOD2, normalize to the expression of hypoxanthine phosphoribosyl transferase 1 (HPRT1) in the TCPS control. The results were representative of three independent experiments.

Table 4. Primer sequences for RT-qPCR

Gene Symbol	Direction	Primer sequence (5'- 3')
NQO1	Forward	TCACCGAGAGCCTAGTTCC
	Reverse	GTGAGCCAGTACGATCAGTG
SOD1	Forward	TGAAGGTGTGGGGAAGCATT
	Reverse	AGTCTCCAACATGCCTCTCTTC
SOD2	Forward	GACAAACCTCAGCCCTAACG
	Reverse	CTGCAGCTTCTCCTTAAACTTG
HPRT1	Forward	GCTGACCTGCTGGATTACAT
	Reverse	CCCTGTTGACTGGTCATTACA

3.2.10 Immunofluorescence Image Analysis

Image analysis was conducted using Fiji (ImageJ) software, and all images in a single channel were merged using the Z-project option (maximum intensity projection). Further adjustments to brightness and contrast were made using the same software. For cell quantification using raw images, Fiji was used. The cell population was quantified by manually adjusting the threshold to remove background from different channels, and the stained cells were measured using the "analyze particle" option.

3.2.11 Statistical Analysis

The quantitative analysis was conducted using ImageJ software, while the statistical analysis was performed using GraphPad Prism (version 9.5.1). To determine the statistical significance of multiple comparisons, one-way ANOVA with Tukey's post hoc test was employed, and the significance threshold was set at $P \leq 0.05$. All data are presented as means ± standard deviation (SD). Each experiment was repeated at least three times to ensure robustness and reproducibility ($n \geq 3$).

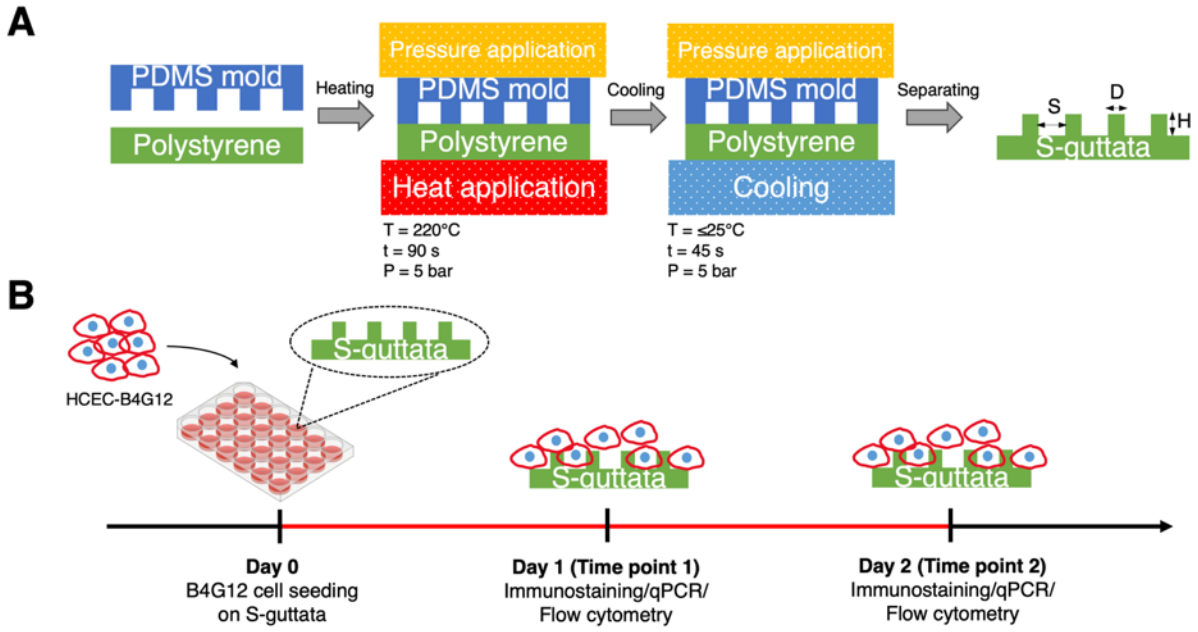
The statistical comparison between the S-guttata pillars and the unpatterned (UP) control, as well as the tissue culture plates (TCPS), was carried out using one-way ANOVA with Tukey's post hoc test. A significant difference was considered when the p-value was less than 0.05 ($p < 0.05$).

3.3 Results

3.3.1 Fabrication and Characterization of Polystyrene S-guttata Pillars

Heat embossing approach was used to fabricate patterned topographic on tissue culture polystyrene (TCPS) surfaces. The fabrication process for S-guttata pillars substrates is summarized in **Scheme 1A**. The decision was made to utilize an embossing temperature higher than the glass transition temperature of polystyrene to facilitate the movement of polystyrene into the predefined

patterns of the master mold. Achieving distortion-free features was determined to be dependent on the cooling of the embossed TCPS and subsequent separation from the PDMS master mold at room temperature. **Figure 5A** displays the reflected confocal laser scanning microscope images of the patterned TCPS surfaces. While the replicated features exhibited a little larger size compared to the original design (**Table 5**), the replication process consistently produced precise and reproducible results **(Figure 5B)**.



Scheme 1. Experimental design of the study.
(A) Hot embossing steps of S-guttata pillars. S: spacing; D: diameter; H: height. (B) Schematic illustration of the experimental design for cell apoptosis and imaging using S-guttatas.

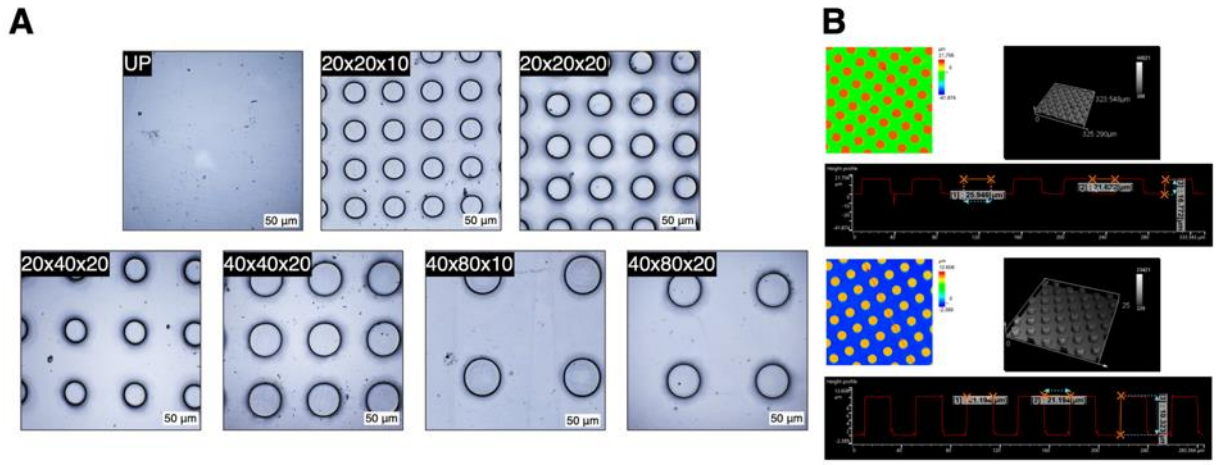


Figure 5. Reflected confocal laser scanning microscope images of different S-guttatas and UP. (A) Representative images of S-guttatas, UP has no topographical structures and used as a control. Scale bar 50 µm. (B) Profile measurement of 10 and 20 µm height S-guttata as an example of representative S-guttata. Diameter, spacing and height measured after fabrication. UP = unpatterned hot embossed polystyrene.

Table 5. Profile measurement of S-guttata pillars micro-structures used for studying cell apoptosis

Patterns	Distance (µm)	Spacing (µm)	Height (µm)
20x20x10	21.14	21.19	10.12
20x20x20	21.07	21.73	19.31
20x40x20	42.66	23.00	18.30
40x40x20	40.06	45.07	18.64
40x80x10	81.61	45.75	10.90
40x80x20	82.54	44.51	19.10

3.3.2 S-guttata Pillars Induced Early Apoptosis

The experimental design for cell apoptosis study on S-guttata is summarized in **Scheme 1B**. Early apoptosis of B4G12 cells was examined by Annexin V-FITC and Propidium Iodide (PI) staining at high cell density (3000 cells/mm^2) and low cell density (1000 cells/mm^2) seeding. **Figure 6A** shows immunofluorescence staining images of B4G12 cells on S-guttata pillars following 1 and 2 days. Green fluorescent label indicates Annexin V$^+$ cells, while red fluorescent label indicates PI$^+$ cells and counterstained with blue-fluorescent DNA stain (DAPI). The apoptotic

rate of B4G12 cells was found to be significantly higher on 20x20x20 when compared to an unpatterned TCPS (UP) control substrate and rest of the pillars at day 1 (**Figure 6A** and **6B**, $p < .001$). Whereas all pillars showed a significant difference ($p < .001$) against the UP at day 2. Comparing among the pillars, cells on 20x20x20 were highly apoptotic compared to 20x40x20 and 40x80x20 (**Figure 6A** and **6B**, $p < .001$ and $p = 0.016$). In contrast, 20x40x20 had the lowest apoptotic rate and was significantly lower than 40x40x20 (**Figure 6A** and **6C**, $p = 0.022$) at day 2. There was no significant difference among other the pillars at day 1 and day 2. In terms of guttata touching cells, Annexin V^+ cells on 20 µm diameter S-guttata pillars (20x20x10, 20x20x20 and 20x40x20) were touching pillars after day 1 (**Figure 6B**). Approximately 50% of cells positive for Annexin V-FITC were observed to be located within the gaps between the pillars in the higher diameter S-guttata pillars structures (40x40x20, 40x80x10, and 40x80x20). A similar phenomenon was observed on day 2, with the lowest percentage of S-guttata pillars touching cells observed on the 20x40x20 (**Figure. 6C**).

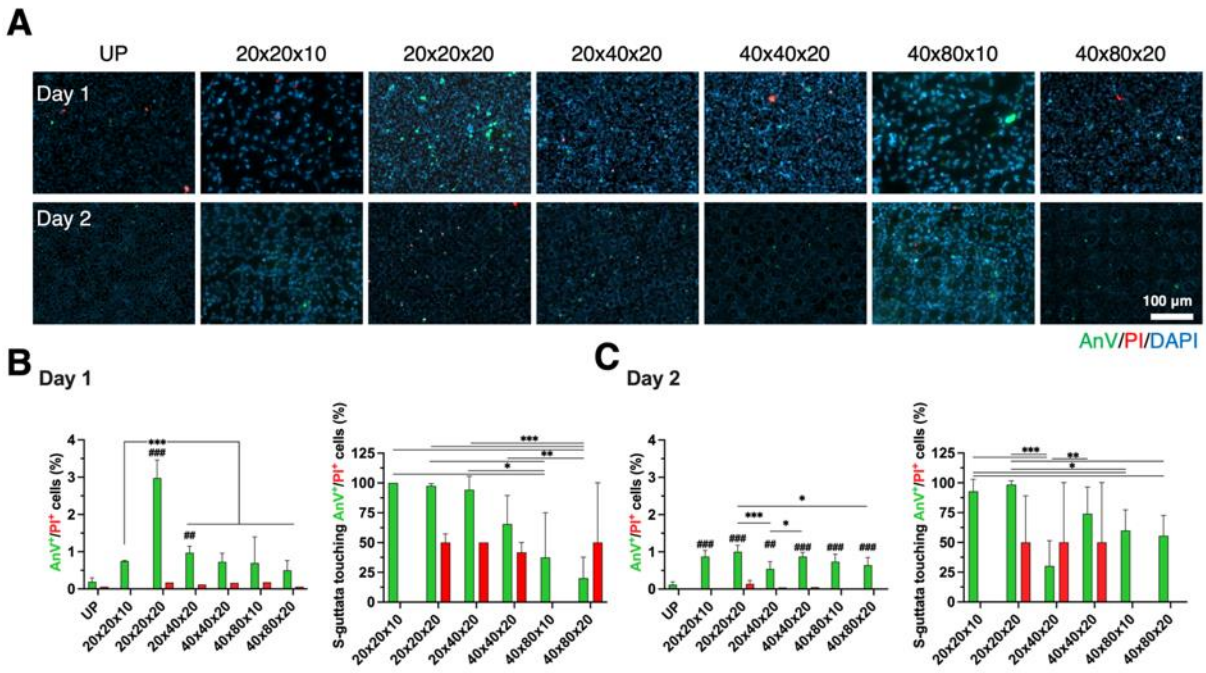


Figure 6. Immunofluorescence staining of early apoptotic cells on S-guttata pillars using Annexin V and propidium iodide (PI) with high cell density.
(A-C) Representative images of apoptotic cells detected by Annexin V and PI staining and counterstained for DAPI after 1- and 2-days culture on S-guttata pillars. Green fluorescence indicates Annexin V binding to phosphatidylserine (PS) on the outer leaflet of apoptotic cells, while red fluorescence represents PI staining of necrotic cells with compromised plasma membrane integrity. Scale bar 100 μm. (B-C) Quantification of apoptotic and necrotic cells, and S-guttata pillars touching positive cells. The graph shows the percentage of Annexin V-positive cells (apoptotic) and PI-positive cells (necrotic) relative to the total cell population. Data are presented as mean ± standard deviation (n = 3). # and * indicates that there is a significant difference between S-guttata pillars versus UP control and between S-guttata pillars, respectively. One, two and three symbols indicate $p < 0.05$, 0.01, and 0.001, respectively. UP = unpatterned hot embossed polystyrene.

To accurately assess cell apoptosis, flow cytometry analysis was performed utilizing Annexin V-FITC and Propidium iodide (PI) staining, which provided enhanced sensitivity and specificity. For the control groups, the results indicated a low percentage of apoptotic cells on negative control, and high percentage of dead cells on positive control. At day 1, all 20 μm height pillars showed higher rate of apoptotic cells compared to UP control; however, there was not statistically significant (**Figure 7** and **Figure A1**). While cells on 20x20x20 exhibited a dramatic increase in the percentage of total AnV^+ cells (9.4% ± 2.2%), indicating enhanced early apoptosis on day 2 (**Figure 7** and **Figure A2**). Cell apoptosis was enhanced across all pillars at day 2, with a notable increase observed in the total number of Annexin V-positive (AnV^+) cells on the 20x40x20 and 40x80x10 pillars (**Figure 7** and **Figure A2**) compared to UP control. Thus, examination was specifically focused on 20 μm height pillars with low seeding cell density, which also to reflect the relatively a smaller number of cells present during late stage FED.

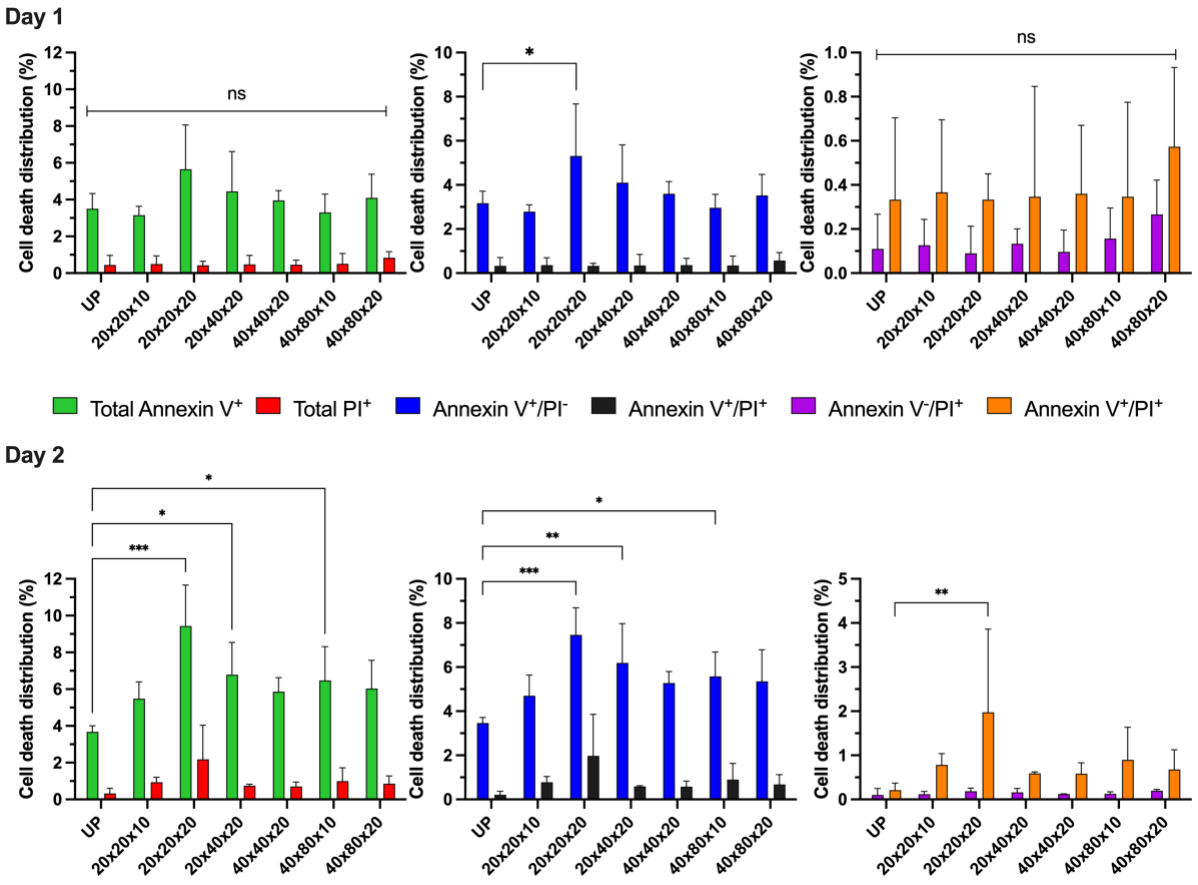


Figure 7. Assessment of S-guttata pillars induced apoptosis on S-guttata pillars using Annexin V and propidium iodide (PI) staining by flow cytometry with high cell density.
Quantification of cell populations based on Annexin V and PI staining. Data are presented as mean ± standard deviation (n = 3). One, two and three symbols indicate $p < 0.05$, 0.01, and 0.001, respectively. UP = unpatterned hot embossed polystyrene.

Among the different S-guttata pillar tested with low cell seeding density, 1000 cells/mm^2, 20x20x20 consistently exhibited the highest level of cell apoptosis at both day 1 and day 2 (**Figure 8**). Additionally, greater cell apoptosis was observed across all pillars compared to the unpatterned (UP) control. The presence of pillars contributed to increased apoptosis compared to the UP control. Notably, more than 90% of the cells were found in close proximity to the pillars on 20x20x20 and greater than 50% of cells were located nearby on pillars on rest of S-guttata pillars (**Figure 8B and 8C**). These findings suggest that the pillar size and spacing influence cell apoptosis, with the 20x20x20 pillars showing the highest apoptotic response.

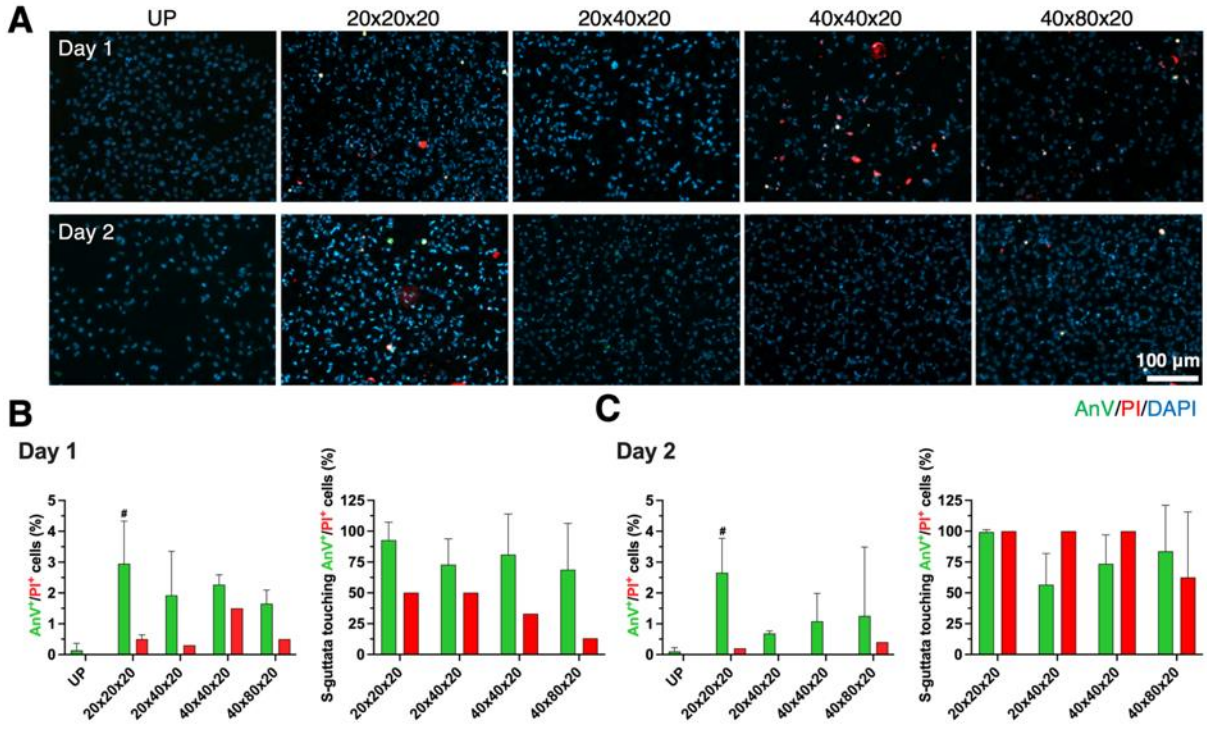


Figure 8. Immunofluorescence staining of early apoptotic cells on S-guttata pillars using Annexin V and propidium iodide (PI) with low cell density.

(A-C) Representative images of apoptotic cells detected by Annexin V and PI staining and counterstained for DAPI after 1- and 2-days culture on S-guttata. Green fluorescence indicates Annexin V binding to phosphatidylserine (PS) on the outer leaflet of apoptotic cells, while red fluorescence represents PI staining of necrotic cells with compromised plasma membrane integrity. Scale bar 100 µm. (B-C) Quantification of apoptotic and necrotic cells, and S-guttata touching Annexin V-positive cells. The graph shows the percentage of Annexin V-positive cells (apoptotic) and PI-positive cells (necrotic) relative to the total cell population. Data are presented as mean ± standard deviation (n = 3). # indicates that there is a significant difference against UP control. One, two and three symbols indicate $p < 0.05$, 0.01, and 0.001, respectively. UP = unpatterned hot embossed polystyrene.

3.3.3 Col5A1 Coated S-guttata Pillars Induced Early Apoptosis

As observed previously, S-guttata pillars induce a higher rate of early apoptosis, particularly in small S-guttata (20x20x20) compared to other S-guttatas and the UP control. To gain a better understanding of the effects of guttatas on cell apoptosis, we selected two S-guttata pillars, small (20x20x20) and large (40x80x20), for Col5A1 protein coating and examined early apoptosis. After two days, cells on both Col5A1 protein-coated and non-coated small pillars (20x20x20) exhibited

a similarly high rate of AnV+ cells (11.5% ± 4.1%) and (12.6% ± 7.2%), respectively. In contrast, Col5A1 protein enhanced cell apoptosis with 13.3% ± 3.4% on the large pillar (40x80x20) after two days compared to the non-coated large pillar and the UP control (**Figure 9A** and **B**). There were no significant differences in terms of PI^+ cells among S-guttata pillars and compared to UP control.

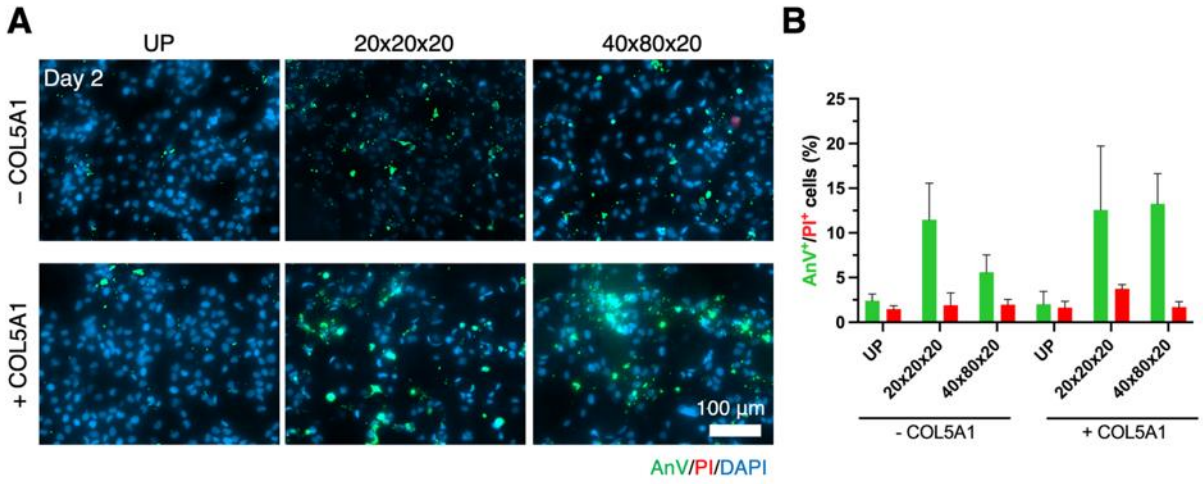


Figure 9. Immunofluorescence staining of early apoptotic cells on Col5A1 coated S-guttata pillars using Annexin V and propidium iodide (PI) with high cell density.
(A) Representative images of apoptotic cells detected by Annexin V and PI staining and counterstained for DAPI after 2-days culture on Col5A1 coated S-guttata. Green fluorescence indicates Annexin V binding to phosphatidylserine (PS) on the outer leaflet of apoptotic cells, while red fluorescence represents PI staining of necrotic cells with compromised plasma membrane integrity. Scale bar 100 µm. (B) Quantification of apoptotic and necrotic cells. The graph shows the percentage of Annexin V-positive cells (apoptotic) and PI-positive cells (necrotic) relative to the total cell population. Data are presented as mean ± standard deviation (n = 3). UP = unpatterned hot embossed polystyrene.

3.3.4 S-guttata Pillars Induced Late Apoptosis

To test whether S-guttata pillars further induces late apoptosis, cells were stained with a terminal deoxynucleotidyl transferase dUTP nick end labeling (TUNEL) assay kit (**Figure 10** and **Figure 11A**) after 2 days. Extreme amount of $TUNEL^+$ apoptotic cells were detected on 20 µm height pillars, while total number of $TUNEL^+$ cells were low on 10 µm height pillars (**Figure 10**

and **11A**). Regarding interaction between S-guttata pillars and B4G12 cells, more than half of the $TUNEL^+$ cells were found to be in contact with pillars in structures with spacing of ≤ 40 μm (20x20x10, 20x20x20, and 20x40x20) (**Figure 11B**). Conversely, approximately 50% of the $TUNEL^+$ cells were observed within the gaps between the pillars in the higher spacing 80 μm S-guttata pillars structures (40x80x10 and 40x80x20) on both experimental days (**Figure 11B**). These findings indicate an enhanced level of late apoptotic cell death on 20 μm height pillars, implicating its role in the regulation of late apoptosis in B4G12 cells.

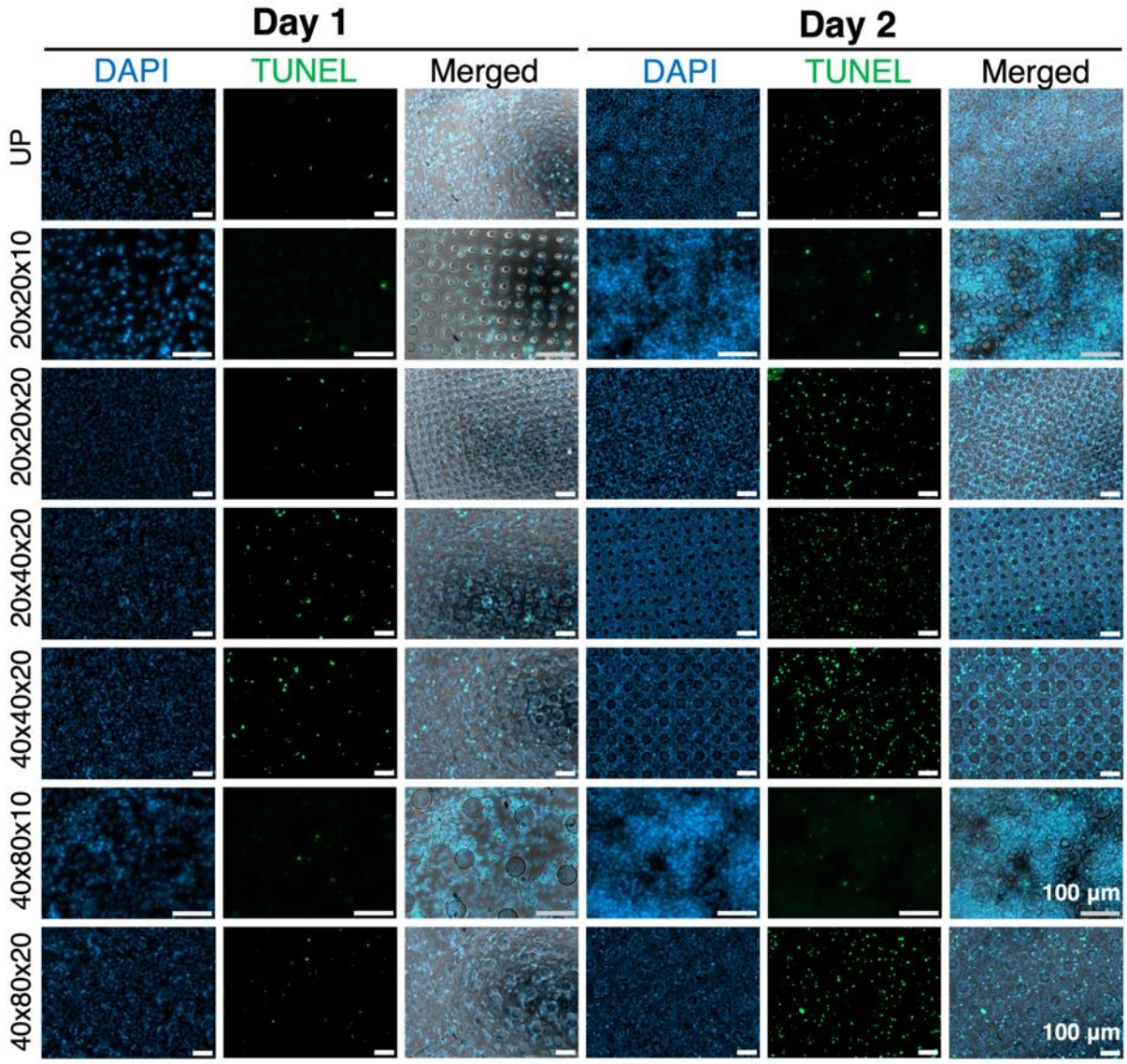


Figure 10. Detection of DNA fragmentation on S-guttata pillars using Terminal deoxynucleotidyl transferase-mediated dUTP nick end labeling (TUNEL) assay. Representative images of TUNEL staining and counterstained for DAPI. After 1- and 2-days culture on S-guttata pillars. Green fluorescence indicates TUNEL-positive cells with fragmented DNA. Scale bars 100 µm.

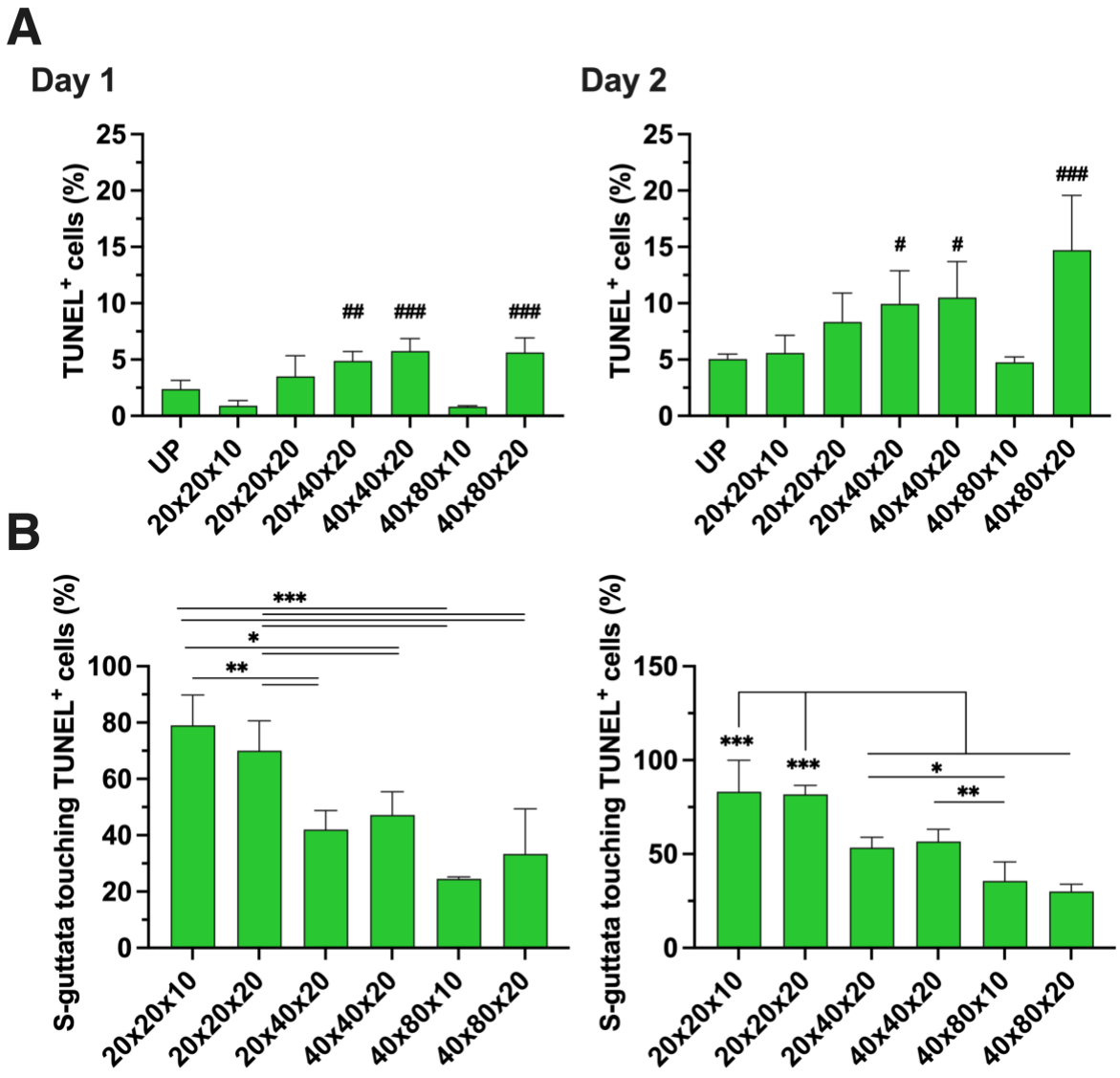


Figure 11. Quantification of TUNEL-positive cells on S-guttata pillars and pillars touching TUNEL-positive cells.

(A) The graph shows the percentage of TUNEL-positive cells relative to the total cell population and (B) S-guttata pillars touching TUNEL-positive cells after 1 and 2 days on S-guttata pillars. Data are presented as mean ± standard deviation (n = 3). # and * indicates that there is a significant difference between S-guttata pillars versus UP control and between S-guttata pillars, respectively. One, two and three symbols indicate $p < 0.05$, 0.01, and 0.001, respectively. UP = unpatterned hot embossed polystyrene.

3.3.5 Cytoskeletal Stress Induced by S-guttata Pillars

To assess the potential induction of cytoskeletal stress on B4G12 cells by S-guttata pillars during cell apoptosis, two types of pillars were specifically chosen, one set with a diameter and

spacing of 20 µm and another set with a diameter of 40 µm and 80 µm spacing. The number of α-SMA positive cells were quantified (**Figure 12).** When compared to the UP control, S-guttata pillars induced a noticeable increase in the α-SMA expression, particularly in cells that were in direct contact with the S-guttata pillars (**Figure 12C**). For instance, among the examined patterns, more than 60% of cells expressing α-SMA were observed to be in contact with S-guttata pillars such as 20x20x10, 20x20x20, and 40x80x10. Conversely, approximately 30% of α-SMA^{+} cells were found to be in contact with S-guttata pillars on 40x80x10 (**Figure12A** and **C**); notably, this pattern exhibited the highest percentage of α-SMA-positive cells among all the studied patterns.

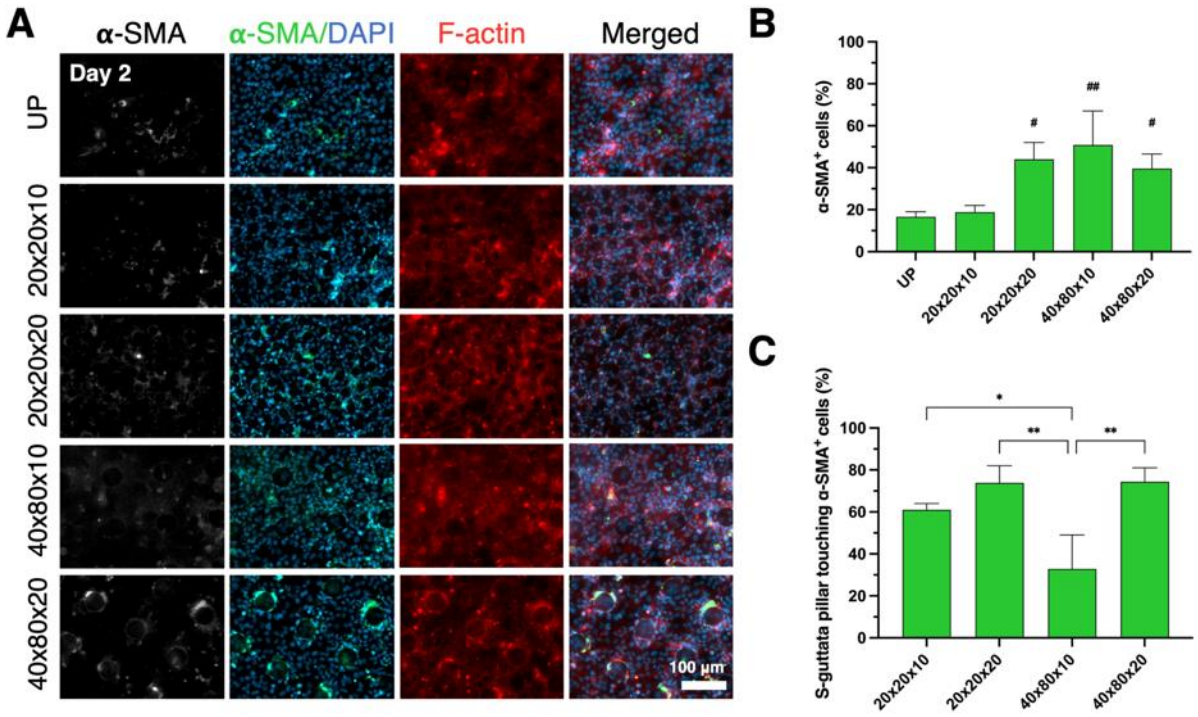


Figure 12. Cell contractility on S-guttata pillars
(A) Immunofluorescence staining of alpha smooth muscle actin (α-SMA) expression on B4G12 cells on S-guttata pillars. Representative images of B4G12 cells on S-guttata pillars after 2-days culture showing α-SMA expression. Green fluorescence indicates α-SMA-positive cells and counterstained for DAPI (blue) and phalloidin (red). Scale bar 100 µm. (B) Quantification of α-SMA-positive cells and (C) S-guttata pillars touching positive cells at day 2. The graph shows the percentage of α-SMA-positive cells relative to the total cell population after 2 days on S-guttata pillars. Data are presented as mean ± standard deviation (n = 3). # and * indicates that there is a significant difference between S-guttata pillars versus UP control and between S-guttata pillars,

respectively. One, two and three symbols indicate $p < 0.05$, 0.01, and 0.001, respectively. UP = unpatterned hot embossed polystyrene.

Another marker is pMLCK for cell contractility, and the expression level of pMLCK was examined **(Figure 13**) following two days. There was no significant difference in total pMLCK expression level between the S-guttata pillars and UP, nor between the S-guttata pillars themselves at day 2 (**Figure 13B**). While cells around S-guttata pillars expressed significant level of pMLCK ($p < .001$), particularly cells adjacent to 20 μm height S-guttata-pillars compared to the 10 μm height S-guttata-pillars (**Figure 13C**). These results indicated that height of S-guttata-pillars are crucial factor to modulate cell contractility for apoptosis.

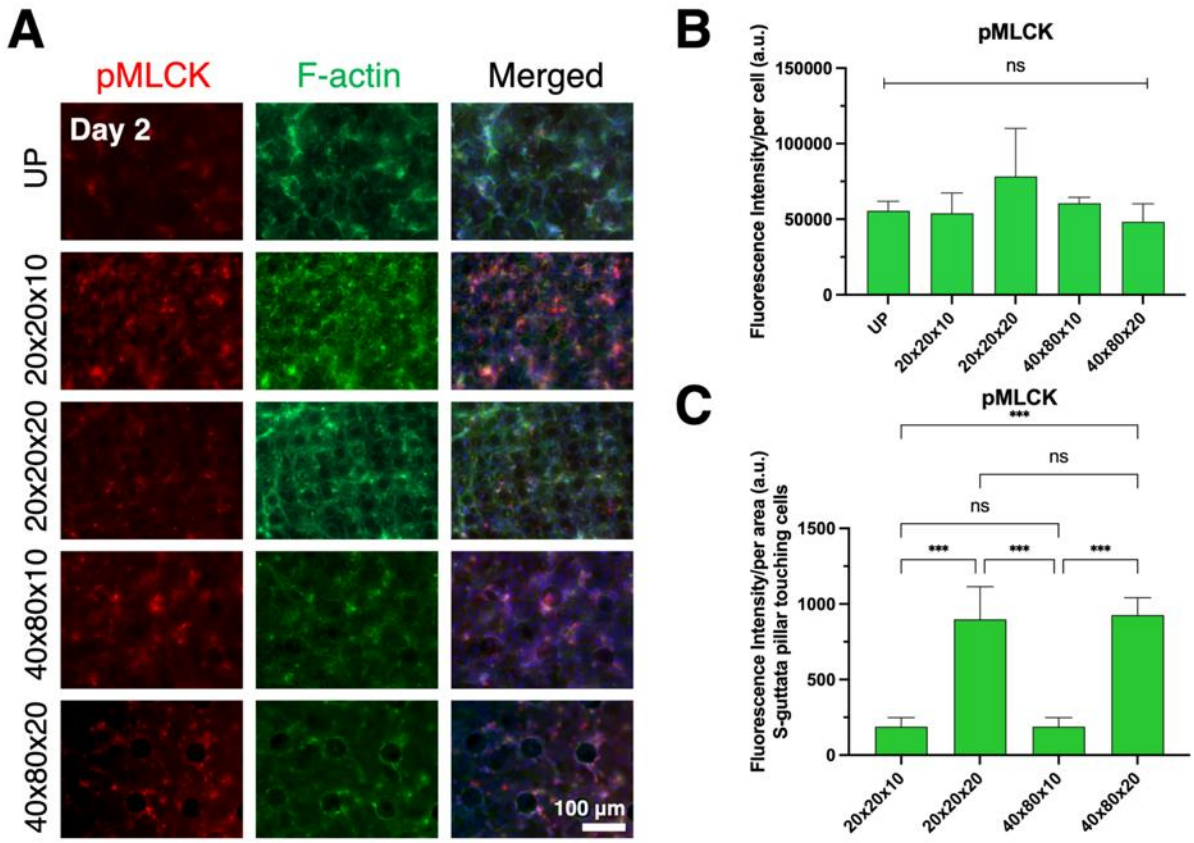


Figure 13. Phospho-Myosin Light Chain 2 (pMLCK) expression on S-guttata pillars (A) Immunofluorescence staining of pMLCK expression on B4G12 cells on S-guttatas. Representative images of B4G12 cells on S-guttata after 2-days culture showing pMLCK expression. Red fluorescence indicates pMLCK cells and counterstained for DAPI (blue) and phalloidin (green). Scale bar 100 μm. (B) Fluorescent intensity per cell and (C) S-guttata touching

cells. Data are presented as mean ± standard deviation (n = 3). Scale bar = 100 µm. One, two and three symbols indicate $p < 0.05$, 0.01, and 0.001, respectively. UP = unpatterned hot embossed polystyrene.

3.3.6 Oxidative Stress Gene Expression on S-guttata Pillars

To assess oxidative stress levels in cells on S-guttata pillars, we evaluated the expression of three genes involved in cellular oxidative stress including NQO1, SOD1, and SOD2. Menadione (MN) and tert-Butyl hydroperoxide (tBHP) were used to induce oxidative stress in cells and effective concentrations were determined with titration assay (**Figure A4**). After two days on 40 µm S-guttata pillars, NQO1 expression showed upregulation compared to both the 20x20x20 pillar and the UP control (**Figure 14**). However, there was no significant difference observed in SOD1 expression between the pillars and the UP control (**Figure 14**). Interestingly, the 20x20x20 pillars downregulated the expression of SOD2 in B4G12 cells, while the 40x80x20 pillars upregulated SOD2 expression after two days (**Figure 14**). These findings suggest that 20 µm height S-guttata pillars can modulate the expression of NQO1 and SOD2 genes.

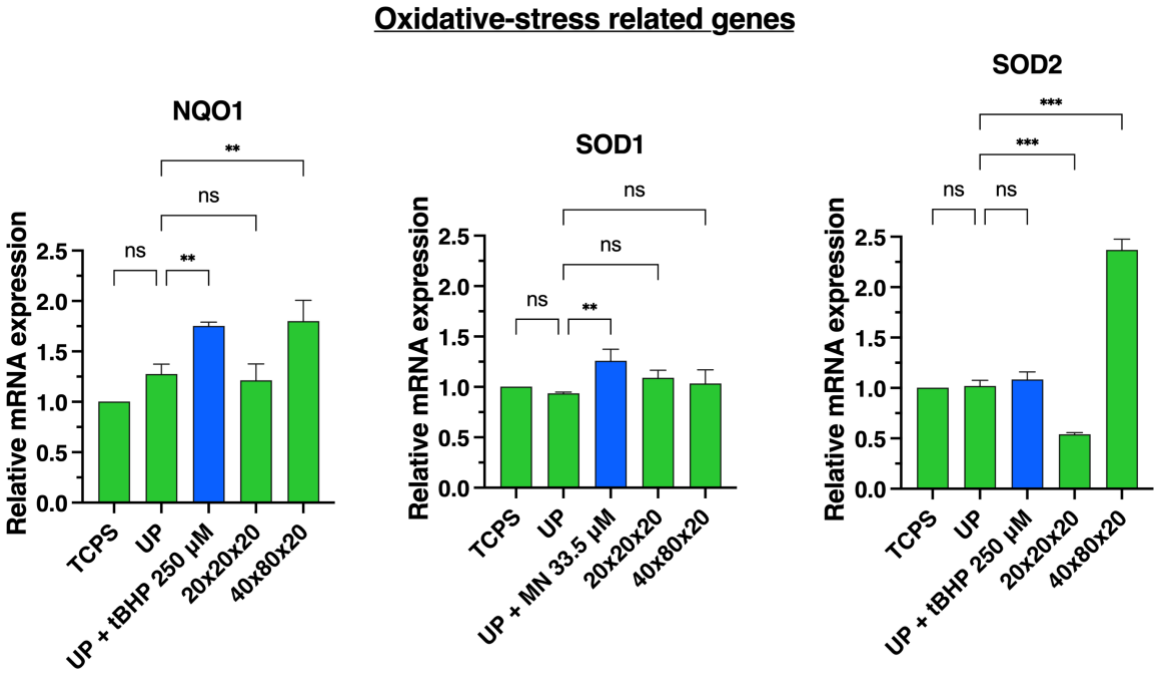


Figure 14. Relative mRNA expression of NQO1, SOD1 and SOD2 genes on S-guttata following two days.
RT-qPCR analysis showed expressions relative to TCPS and compared to UP control for NQO1, SOD1, and SOD2 genes. Data were normalized to HPRT1 expression. One, two and three symbols indicate $p < 0.05$, 0.01, and 0.001, respectively. Data are presented as mean ± standard deviation ($n = 3$). UP = unpatterned hot embossed polystyrene.

3.4 Discussion and Conclusion

3.4.1 Corneal guttata and cell apoptosis

In this study, we used previously developed S-guttata pillars to study corneal endothelial cell apoptosis [43]. The S-guttata models were selected based on the clinical observations and from published literatures [40, 76, 82, 89-92]. Guttata, small excrescences found on the DM of the cornea, have been involved in the pathogenesis of FED. These excrescences are often seen as tiny, round, or oval spots when viewed through a slit lamp microscope [65, 93]. Guttata have been associated with inducing cell apoptosis, a key process that contributes to the degeneration of corneal endothelial cells in FED patients [26, 40]. Guttata known as an abnormal collagen deposition [83, 85], secreted by abnormal corneal endothelial cells and may appear as a result of aging. For example, collagen type I, II, III, IV, V and VIII are highly expressed in human corneal guttatas [86, 87]. Depending on the stage or advancement of FED, guttata can exhibit a broad spectrum of dimensions in diameter, spacing and heights [76]. Therefore, our S-guttata model encompassed diverse topographical parameters, including diameter, spacing, and height of the guttata from 10 – 80 microns. Moreover, we also tested the effect of Col5A1, which is one of the highly expressed proteins in corneal guttata [86], by coating S-guttata with Col5A1 human recombinant protein. The design of the study also allowed us to examine guttata induced corneal endothelial cell apoptosis comprehensively.

Cell apoptosis, senescence, and activation have been observed in FED endothelium, suggesting that they are the primary contributors to dysfunction in DM. We have presented a

comprehensive investigation into the impact of S-guttata with varying dimensions, designed to mimic distinct stages of FED, on cell apoptosis. When cells encountered small S-guttata patterns (20 μm diameter and height), they exhibited higher levels of early apoptosis compared to lower height pillars (10 μm height) and unpatterned control. In particular, 20x20x20 and 20x40x20 induced higher rate of cell early apoptosis due to the remodeling their actin cytoskeleton [94].

Changes in the ECM composition of DM has also been observed in FED. The normal DM and the extra layers 3 and 4 exhibited identical collagen types, as confirmed by analyzing their amino acid composition [95]. Altered ECM protein expression in DM was reported in number of studies [96, 97]. Thus, we examined the effect of one of the ECM proteins Col5A1 on cell early apoptosis. Significantly, Col5A1 protein was able to upregulate cell early apoptosis by 7.7% when coating on large S-guttata (40x80x20) (**Figure 9B).** However, cell apoptosis rate was the same on small S-guttata (20x20x20) after coating with Col5A1 protein (**Figure 9**). These findings revealed that ECM composition plays a vital role during FED for cell apoptosis.

Fuchs' dystrophy has been extensively studied among corneal dystrophies but traditional techniques such as light microscopy and transmission electron microscopy (TEM) have not clearly identified late apoptotic endothelial cells in FED [18, 98]. In 2000, Borderie *et al.* showed that in FED samples, endothelial cell apoptosis was evident through various indicators such as condensed nuclei, reduced cell size, positive TUNEL labeling, and DNA fragmentation, observed in 79% to 100% of the cases [40]. In our study, we observed that large S-guttata with 40 μm diameter pillars induced a higher incidence of late apoptosis in B4G12 cells compared to smaller 20 μm diameter pillars and unpatterned controls (**Figure 10** and **11**). Interestingly, only small portion of the TUNEL-positive cells adjacent to the pillars, which may indicate that cells only came into physical contact with the pillars during their lifetime. However, we did observe apoptotic cells situated

between individual pillars, suggesting that these cells may have interacted with the guttata pillars during their cellular lifespan, potentially contributing to apoptotic signaling cues.

S-guttata FED disease model was developed on a patient's guttata parameters to study *in vitro* cell apoptosis induced by S-guttata. Our findings highlighted the influence of S-guttata pillars on apoptosis induction, with guttata density and pillar height playing crucial roles in cell apoptosis. Particularly, small S-guttata, 20 μm diameter, spacing and height induces early apoptosis, and large S-guttata, 40 μm diameter, 80 μm spacing and 20 μm height S-guttata induces late apoptosis. Although the transition between from early to late apoptosis may not always be clearly defined.

3.4.2 Corneal guttata and Cell contractility

During apoptosis, cells undergo contraction, accompanied by an increase in MLCK phosphorylation, facilitating the formation of blebs as part of the apoptotic process [99, 100]. The intricate relationship between these dimensional variations and their influence on cytoskeletal dynamics could ultimately culminating in cellular apoptosis [94, 101]. The increased cytoskeletal stress resulting from the interaction between S-guttata pillars, and the cells appears to correlate with the higher α-SMA expression and pMLCK expression. Since during cell apoptosis, cell cytoskeleton changes and cells become rounder [102] along with actin reorganization, and stress fibers loss [103, 104]. Particularly, cells nearby S-guttata pillars on 20 μm height pillars expressed substantial amount of the cell contraction markers due to the physical interactions with pillars walls (**Figure 13C**). Furthermore, observing apoptosis occurring on S-guttata pillars, a significant proportion of apoptotic cells were found to be nearby S-guttata pillars with 20 μm height pillars, as opposed to those on 10 μm height pillars.

Alpha-smooth muscle actin (α-SMA) is a protein that is typically expressed in smooth muscle cells, myofibroblasts, and pericytes [105]. It plays a crucial role in cell contractility and is often

used as a marker to identify myofibroblast differentiation, which is associated with tissue remodeling, wound healing, fibrosis and lead to cell apoptosis [106]. Fibroblastic phenotype changes observed, specifically on large S-guttata (40x80x10 and 40x80x20) near pillars which indicate significant influence of S-guttata pillars on cellular behavior (**Figure 12C**). These results suggested that S-guttata pillars can induce a localized upregulation of α-SMA expression in corneal endothelial cells, potentially through mechanotransduction mediated pathways [107]. Further investigations into the specific mechanistic pathways involved and the functional consequences of altered α-SMA expression in response to pillar geometry are helpful to elucidate the underlying mechanisms for FED.

3.4.3 Corneal guttata and oxidative stress

As FED advances, a spectrum of alterations come into play, encompassing shifts in factors like oxidative stress, genetic mutations, and the emergence of guttatas [20, 108]. There is abundant evidence indicating that oxidative stress is a significant contributor to the development of FED [21, 109, 110]. The production of reactive oxygen species (ROS) within cells, including superoxide anion, hydrogen peroxide, hydroxyl radical, and nitric oxide, is balanced by inherent antioxidant defense mechanisms. The CECs rely on enzymatic antioxidant systems such as SODs, catalase, glutathione-s-transferases, and peroxidases to combat oxidative stress. Studies have shown downregulation of antioxidant genes NQO1 and SODs in FED samples compared to normal controls [20, 111]. Interestingly, small S-guttata pillars (20x20x20) were found to significantly downregulate SOD2 expression ($p < 0.001$) at day two, potentially indicating oxidative stress in cells and leading to cell apoptosis (**Figure 10** and **11A** and **14**). While, large S-guttata pillars (40x80x20) significantly upregulated SOD2 expression ($p < 0.001$) after two days (**Figure 14**) in

comparison to 20x20x20 and UP. There was not change for SOD1 expression after two days on S-guttata pillars compared to UP.

This suggests that the SOD1 gene may be indirectly involved in cell oxidative stress compared to the SOD2 gene in corneal guttata-induced oxidative stress. Recent studies indicates a potential involvement of reactive estrogen quinones in the development of FED [112]. NQO1 plays a crucial role in converting estrogen quinones back to catechol estrogens [113], which can be further neutralized by catechol-O-methyltransferase (COMT), thus serving as part of the cellular antioxidant defense mechanism [114]. Regarding NQO1 gene expression, cells cultured on 40x80x20 pillars exhibited upregulation of NQO1 following two days, potentially explaining the higher rate of late apoptosis observed on large S-guttata pillars. Conversely, no significant changes were observed on 20x20x20 pillars.

Overall, the study demonstrates that the interaction between corneal endothelial cells and S-guttata triggers both early and late apoptosis, as evidenced in an *in vitro* FED model. Moreover, it emphasizes the significant roles played by cell contractility and fibrogenesis in driving apoptosis, alongside the induction of oxidative stress by guttata in CECs. Importantly, the increased expression of ECM proteins in larger guttata enhances early apoptosis when combined with larger S-guttata, highlighting the importance of guttata dimensions and ECM proteins in corneal endothelial cell apoptosis.

Chapter. 4 Mechanical Properties of Human Descemet's Membrane

4.1 Introduction

Descemet's Membrane (DM) is developed during fetal development, and endothelial cells continually contribute a small quantity of material over a lifetime, resulting in a gradual thickening of the DM, which adopts the characteristics of a basement membrane [115]. Examining the properties and thickness of DM could be crucial for gaining a deeper understanding of its role in the development and advancement of FED. Importantly, previous study has shown that multilayered cell clusters and radial cell rows in peripheral area, suggesting a possible migration of less differentiated cells from the corneal periphery to the corneal center area [116]. While peripheral endothelial cells may have limited proliferative capacity, they may hold the potential to undergo division under *ex vivo* conditions where mitogenic inhibitors are absent.

In the cornea, stiffness plays a critical role in influencing various cellular functions, encompassing epithelial cell adhesion and proliferation, limbus cell differentiation, and the proliferation of corneal endothelial cells [117, 118]. As FED primarily impacts the DM and CEC layers [119], investigating the pathological ultrastructure and mechanical characteristics of the DM is crucial for gaining deeper insights into the development of FED. Despite significant advancements in our understanding of FED in recent years, the exact biomechanical processes triggered by FED remain unclear. DM terminus could likely constitute a niche for progenitor cells and potentially serve as a physio-chemotactic guidance system, directing the movement of cells from the inner TZ to the peripheral endothelium [31]. However, the impact of these cues from DM stiffness on HCECs remains largely unknown.

During the disease or injury, changes in ECM stiffness can lead to alterations in corneal cell behavior [118, 120]. Xia *et al.* observed variations in DM stiffness, particularly around the guttata

region, during FED [121]. They studied the structure and mechanical properties of FED-DMs by using quantitative dynamic atomic force microscopy (QD-AFM) to measure the at nano scale. FED-DM was much thicker (21.9 ± 2.4 μm) than the normal DM (18.8 ± 0.2 μm), and even thicker (38.9 ± 1.7 μm) with the guttata. Moreover, under physiological buffer FED-DM stiffness was 1.0 ± 0.7 MPa, while normal DM was 1.8 ± 0.8 MPa. In contrast, Last *et al.* reported a significantly lower elastic modulus of DM, averaging 50 ± 17.8 kPa with a range of 20 kPa to 80 kPa, using AFM with a spherical probe [122]. The stiffness of DM can vary widely, ranging from kPa to GPa, depending on the measurement techniques employed and sample-to-sample variations. Therefore, achieving accurate measurements of the stiffness of DM is essential for elucidating its influence on CECs and CE progenitor cell migration and differentiation.

In this chapter, the actual thickness of human Descemet's Membrane (DM) in different regions including central (CE), peripheral (PE), and transition zone (TZ) regions was determined using a non-destructive measurement approach that we developed. Estimated refractive index (RI) values were back calculated based on a match of DM thickness measurements with cryosectioning and film thickness measurement with a 3D Confocal Laser Scanning Microscope. Additionally, the stiffness of the DM is determined through a three-point bend testing approach.

4.2 Materials and Methods

4.2.1 Human Descemet's Membrane (DM)

Dissected and decellularized human DM tissues from different regions including central (CE), peripheral (PE), and transition zone (TZ) (n = 12, male/female: 7/5; age: 65.5 ± 3.1 years old; age range: years 60 to 75 old) were provided by our collaborates from Singapore Eye Research Institute (**Table 6**). Samples were transported in Optisol-GS (Bausch & Lomb, Bridgewater, NJ, USA) at 4

°C. The study protocol was approved by the University of Waterloo, Institutional Research Board (43952) and carried out in accordance with the tenets of the Declaration of Helsinki.

Table 6. Human Descemet's Membrane sample information.

Number	Sample ID	Patient age	Patient gender
1	3289	69	Male
2	42272	60	Female
3	3449	67	Male
4	6775	68	Male
5	26234	64	Female
6	25149	65	Female
7	4448	75	Male
8	4388	72	Female
9	4444	72	Male
10	4418	62	Female
11	4401	67	Male
12	4450	73	Male

4.2.2 LEXT film thickness measurement

Using the 3D Laser Scanning Microscope (LEXT) equipped with the film thickness function, each specimen of DM was positioned on the microscope stage, with a few drops of PBS added to maintain hydration. Subsequently, the thickness of each DM region was measured using the film thickness function of the LEXT microscope. The obtained thickness values for each region were then recorded and documented for subsequent analysis. Concurrently, brightfield images of each DM region were captured to estimate the RI required for accurate LEXT thickness measurement. Through comparative analysis of the thickness measurements obtained from the LEXT microscope with those derived from the brightfield images, the RI of each DM sample was adjusted to ensure alignment between the two sets of measurements.

4.2.3 Cryosectioning and Toluidine Blue Staining

Human DM tissues for section staining were embedded with optimal cutting temperature (OCT) (Scigen 4583, Fisher Scientific, USA) compound and frozen at −35 °C. Following, OCT embedded DM tissues were sectioned with 6 μm thick using Leica CM 1900 cryostat (Leica Biosystems Inc, Wetzlar, Germany). For Toluidine blue staining, cryosections of 6 μm thickness were fixed in acetone at −20 °C for 15 minutes and after 3 rinses with PBS for 3 minutes each stained with Toluidine blue for 1 min at room temperature. Following, rinsed with DI water for three times and samples were mounted with Permount™ mounting medium and photographed using a bright field microscopy (Axiovert 200, Zeiss GmBH).

After taking images with bright field microscopy, human DM thickness was determined with Fiji (ImageJ) software. The mean of 10 measured values was calculated for each region of interest within the DM sample. Specifically, 10 sections of the DM sample were measured, and the mean of the 10 values obtained from each region was calculated.

4.2.4 Tensile Testing

The mechanical properties of the different regions of DM samples were measured using a two parallel plate compressive system G2 (Cell Scale Biomaterials Testing, Waterloo, Canada) as shown in **Scheme 2.** DM samples (n = 6 for each region) were placed on a fixed flat stage, maintained at room temperature in PBS solution, and a constant force was applied through a circular tungsten microbeam with a length and diameter of 55 and 0.5588 mm, respectively. The microbeams are made from tungsten wire the expected force resolutions and recommended maximum force is Modulus: 411000 MPa, typical force resolution: 34.52 μN, recommended max force 10,536 μN (**Table 7**). The displacement was set at 20% strain, and DM samples were compressed and recovered for 60 seconds, respectively (**Figure A5**), with a constant load rate

applied while recording force and deflection data. Stress-strain curves data were recorded automatically by the software associated with the MicroTester G2 (**Figure A5**). Then we utilized the flexural modulus value at 5 – 10% strain. This data was further analyzed, and Young's modulus (YM) was calculated using the following equations:

$$\text{Strain } (\epsilon) = \frac{L-3000}{3000} \quad \text{Stress } (\sigma) \frac{F_{fibre}}{\text{Thickness x Width}} \quad F_{fibre} = \frac{F_{beam} L}{\Delta d} \quad L = \sqrt{\Delta d^2 + 3000^2}$$

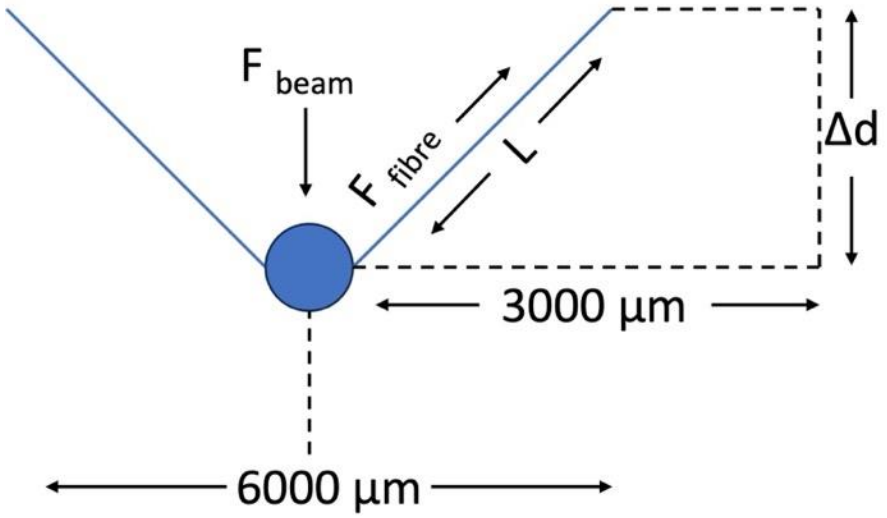
The YM is a measure of material stiffness, where an increase in YM corresponds to increased stiffness or strength of the material. Previously, our lab member (Wesley Luu) determined the stiffness of DM using a MicroTester G2 and calculated YM using the equation:

$$E = \frac{(\sigma)}{(\epsilon)} \quad E = \text{Young's modulus (Elasticity)} \quad \sigma = \text{Stress } \epsilon = \text{Strain}$$

However, the thickness of the DM was measured after testing stiffness, potentially leading to thinning of the DM samples. To address this, we have modified the protocol to measure DM thickness before testing stiffness. This ensures accurate thickness measurement of the DM, which is then used to recalibrate DM stiffness.

Table 7. Expected force resolutions and recommended maximum forces

Diameter (mm)	0.0762	0.1016	0.1524	0.2032	0.3048	0.4064	0.5588	1.0160	1.5748
Modulus (MPa)	411000								
Typical Force Resolution (μN)	0.012	0.038	0.191	0.604	3.056	9.658	34.52	330.54	1907.88
Recommended Max Force (μN)	4	11	57	181	917	2897	10536	99162	572363



Scheme 2. Illustration of 3-point bend test.
Schematic representation of a 3-point bend test setup demonstrating the applied loading configuration on human Descemet's Membrane (DM). The test involves subjecting the material to bending forces at two support points and a central loading point, enabling assessment of DM flexural strength and deformation behavior.

4.2.5 Statistical Analysis

Statistical analysis of different experimental groups was carried out using one-way or two-way ANOVA with Tukey's test. Data were reported as mean ± standard error. Differences with $p < 0.05$ was taken as statistically significant. For DM thickness analysis at least 10 sections ($n \geq 10$) from each region were analyzed. For DM stiffness measurement at least 6 samples ($n \geq 6$) from each region were analyzed.

4.3 Results

4.3.1 Thickness of Human Descemet's Membrane

Three distinct regions including central (CE), peripheral (PE), and transition zone (TZ) of thickness were measured (**Figure 16B**). Each of these zones exhibited variations in thickness, with the CE 14.7 ± 3.6 µm, the PE 6.8 ± 3.7 µm, and the TZ being the thickest at 60.7 ± 7.7 µm (**Figure 16A** and **C**). To measure the accurate thickness of DM by LEXT film thickness function, each

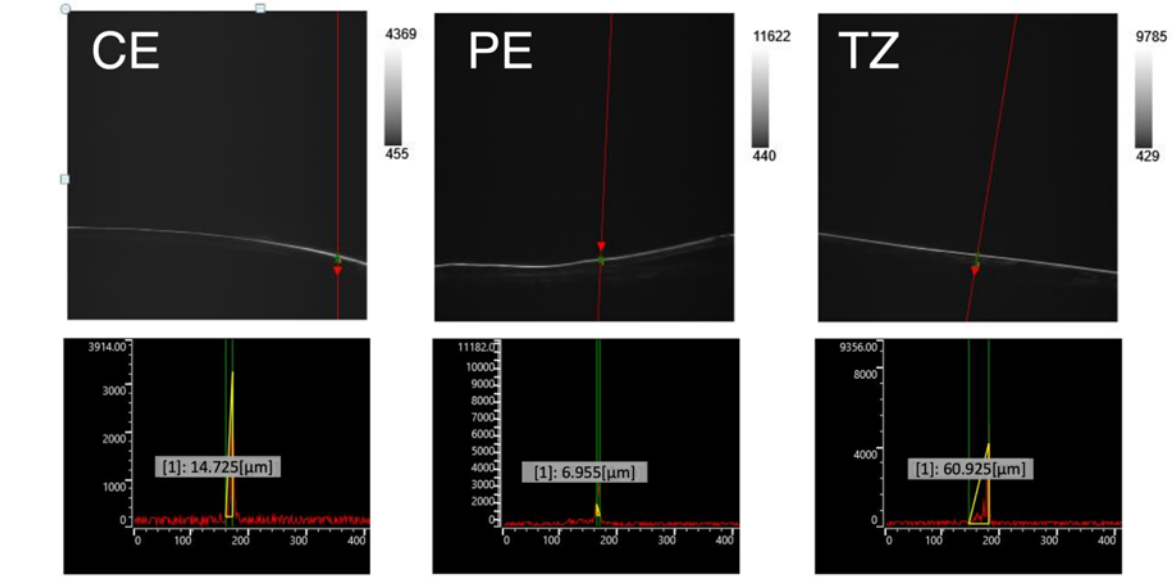
region of DM RI estimated based on thickness matching with brightfield images (**Figure 15A**) (**Table 8**).

Table 8. DM thickness and estimated RI

DM location	Thickness by brightfield microscopy (μm)	Thickness by LEXT (μm)	Estimated RI used for thickness measurement
CE	14.73 ± 3.66	14.7 ± 2.16	1.29
PE	6.88 ± 3.70	6.9 ± 1.21	1.35
TZ	60.72 ± 7.72	60.82 ± 3.88	1.90

To match the thicknesses from microscope images and LEXT measurement, we have adjusted the RI of each sample (**Figure 15**). For example, RI of 1.29, 1.35, 1.90 used to measure the thickness of DM samples with LEXT, respectively (**Figure 15B**). The DM thickness was similar between male and female patient's samples (**Figure A3**). Significantly, the DM exhibited varying levels of thickness across these regions, with the TZ being the thickest, and the PE and CE regions showing progressively lower thickness.

A



B

DM location	Thickness	Refractive index
CE	14.7 ± 2.16	1.29
PE	6.9 ± 1.21	1.35
TZ	60.92 ± 3.88	1.90

Figure 15. LEXT film thickness measurement of representative DM in CE, PE and TZ regions. (A) Thickness of each region were measured with LEXT microscope using film thickness function and (B) RI was estimated based on the match of brightfield image thickness and LEXT measurement.

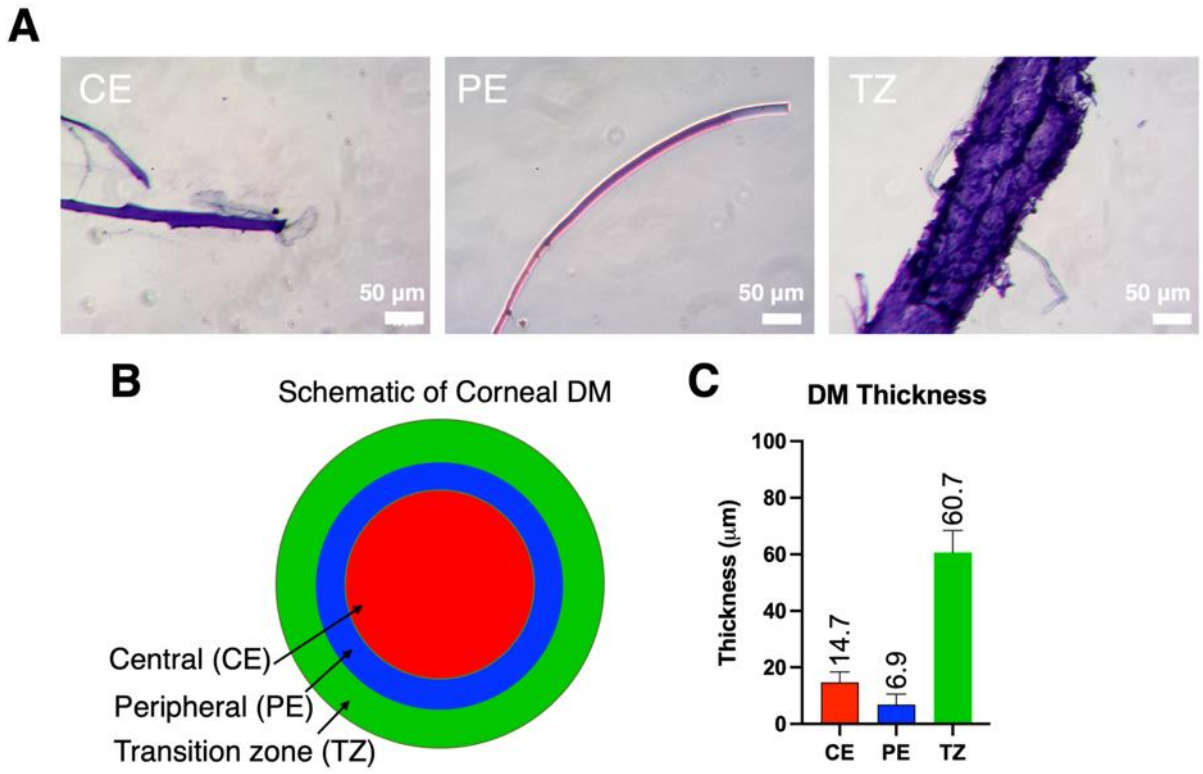


Figure 16. Mechanical property of DM in various regions including Central (CE), Periphery (PE), Transition zone (TZ).
(A) Brightfield imaging of representative DM in CE, PE and TZ regions from male patient's sample. (B) Schematic illustration of corneal DM. (C) Thickness of DM in various regions. Data are presented as mean ± standard deviation (n = 10).

4.3.2 Stiffness of Human Descemet's Membrane

Following thickness measurements, DM stiffness determined by using Microtester with 3 point bend testing. In results, TZ was found the softest tissue compared to the CE and PE (**Figure 17A**). To calculate Young's modulus of DM in each region, DM thickness was calculated with formula stated in section 4.2.3. The observed modulation in DM stiffness as it transitions from TZ to PE suggests the potential presence of CE progenitor cells that undergo slow centripetal migration and differentiation [116]. Additionally, when analyzing the PE/CE ratio was found to be higher in females compared to males (**Figure 17B**). While there was not significant difference in

TZ/CE ratio. This observation suggests a potential indicator for the higher prevalence of female FED cases in the literatures [35, 123].

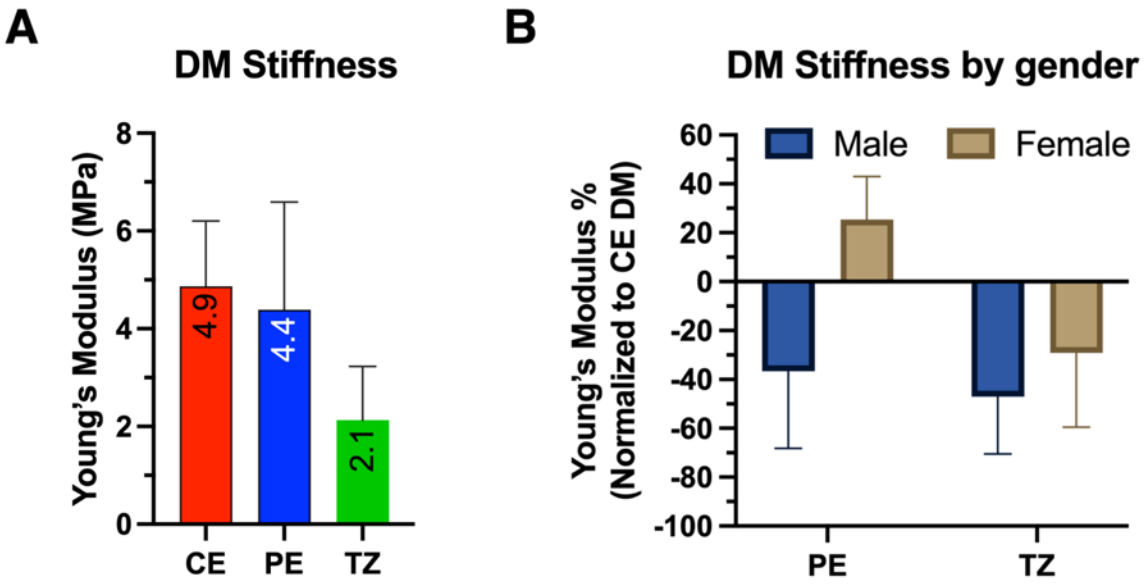


Figure 17. DM stiffness in various regions.
(A) Young's modulus of DM in various regions. Data are presented as mean ± standard deviation (n = 12). (B) Gender comparison for Young's modulus of DM normalized into CE DM. Data are presented as mean ± standard deviation (n = 7 for male and n = 5 for female).

4.3.3 Suggested Protocol for non-destructive measuring DM thickness

To measure the thickness of DM regions accurately, we employed a 3D Laser Scanning Microscope (LEXT) using the film thickness function. First, each DM sample was meticulously positioned on the microscope stage and added few drops of PBS to keep in hydrated state. By the LEXT microscope, we proceeded to measure the thickness of each region separately, using film thickness function that allow us to precisely measure the thickness of the film. Subsequently, we recorded the thickness values obtained for each region, and documenting the data for further analysis. In parallel, brightfield images of each DM region were captured to estimate the refractive index (RI) required for accurate thickness measurement. By comparing the thickness measurements obtained from the LEXT microscope with those derived from the brightfield

images, we adjusted the RI of each DM sample to ensure alignment between the two sets of measurements. This calibration process involved determining RI values that best correlated with the observed thicknesses for each region (e.g., RI of 1.29 for CE, 1.35 for PE, and 1.90 for TZ). These calibrated RI values were then inputted into the LEXT microscope software to account for refractive index variations across different DM regions.

Finally, we verified the adjusted RI values by comparing subsequent thickness measurements obtained with the LEXT microscope to the corresponding brightfield images, ensuring consistency and reliability in the measurement process. Through this newly developed non-invasive protocol, we achieved accurate and reliable measurements of DM thickness across its distinct regions.

4.4 Discussion and Conclusion

4.4.1 Non-invasive approaches for film thickness measurement

In this study, we developed a novel non-invasive methodology to measure the thickness of DM that differs from conventional invasive approaches such as transmission electron microscopy (TEM), atomic force microscopy (AFM) [122, 124], quantitative dynamic atomic force microscopy (QD-AFM) [121], or conventional histological cross-sectional analysis. Traditional methods often involve invasive procedures or destructive sampling [124], which can compromise the integrity of the tissue and limit longitudinal studies [125]. In contrast, our approach focused on non-destructive techniques to accurately measure DM thickness using estimated RI while preserving tissue integrity. LEXT OLS5000 3D Laser Scanning Microscope was utilized, using film thickness function to measure the thickness of the human DM with estimated RI value.

Optical methods are valuable for studying biofilms due to their non-destructive nature and ability to provide non-contact and *in situ* measurements. These techniques include confocal scanning laser microscopy [126, 127], light reflectance-based turbidity measurements [128], photoacoustic spectroscopy [129], and optical coherence tomography [130]. In industrial settings, fiber optic sensors [131] and mechatronic surface sensors [132] are commonly used for real-time monitoring of biofilm development. However, a drawback of traditional imaging techniques is that as higher magnification lenses are utilized to enhance resolution, the field of view becomes narrower. This often necessitates close proximity or contact with the biofilm, potentially altering its natural structure. Wolf *et al.* have discussed the advantages and drawbacks of different optical methods for biofilm monitoring in a comprehensive review [133].

4.4.2 Novel method to measure DM thickness with estimated RI

In the method we have established for DM thickness measurement, firstly, the thickness of DM samples was measured using the 3D Laser Scanning Microscope (LEXT) with the film thickness function. Subsequently, one piece of each sample from different regions underwent cryosectioning and stained with Toluidine blue to accurately measure the thickness of the CE, PE, and TZ, respectively. Once the thickness of each DM region was determined, it was matched with the LEXT thickness measurement by adjusting the refractive index (RI) of the samples. Using these thickness values, the RI of each sample estimated with the film thickness function in the LEXT microscope by back calculating. Following this, another piece of each sample from various regions, including CE, PE, and TZ, was tested for stiffness. The results indicate accurate thickness measurements of the DM in various regions and provide estimations of the RI. Specifically, the RI for the PE and CE regions was consistent with the findings of Lin et al., where the corneal group index was reported as 1.389 ± 0.004 [134]. However, the RI for the TZ was higher at approximately 1.9 compared to PE and CE.

In conclusion the newly developed approach for measuring film thickness in DM offers a comprehensive and accurate methodology. By combining 3D Laser Scanning Microscopy (LEXT) with cryosectioned brightfield images, we were able to precisely measure the thickness of different regions within the DM, including the CE, PE, and TZ. Additionally, our study highlights substantial variations in DM thickness and stiffness across CE, PE, and TZ regions. Moreover, higher PE/CE ratios in females may serve as an indicator for the elevated prevalence of female FED cases. These findings demonstrate the effectiveness of our approach in accurately assessing DM thickness and RI, laying a solid foundation for further research in ocular biomechanics and related fields.

Chapter. 5 General Conclusions

5.1 S-guttata pillars induced cell apoptosis

In conclusion, our synthetic guttata FED disease model based on a patient's guttata parameters was developed to evaluate the comprehensive cell apoptosis and cell cytoskeletal changes induced by guttata-laden surfaces. When B4G12 cells were seeded on high-density S-guttata pillars (20 μm in diameter, spacing, and height), Annexin V^+ cells were observed. Conversely, larger diameter pillars (40 μm) with increased height (20 μm) induced late apoptosis. However, it's notable that half of the total early and late apoptotic cells were not touching to the pillar walls on the larger diameter S-guttata (40 μm). Furthermore, Col5A1 coated larger S-guttata were able to enhance cell apoptosis on large pillars (40x80x20). The signs of fibroblastic phenotype changes have been observed adjacent to S-guttata pillars walls and suggesting the physical presence of the S-guttata pillars influences on cellular behavior and phenotype. Moreover, the principal consequence of increased level of pMLCK nearby pillars wall that observed on small and large S-guttata pillars, leading to membrane blebbing, one of the first events in the execution phase of apoptosis. These results indicate that DM guttata induces the cell early and late apoptosis based on their dimensions. Overall, this study highlights the pivotal role of guttata dimensions in initiating and modulating different stages of cell apoptosis, ultimately contributing to the cell death during FED.

5.2 Mechanical properties of human Descemet's membrane

The accurate thickness of DM was determined by using non-destructive approach before testing the DM stiffness. The TZ exhibited the greatest thickness, while the CE and PE regions displayed progressively lower thickness levels. Moreover, the stiffness analysis indicated that the TZ was the softest tissue compared to the CE and PE regions, suggesting a gradient of mechanical properties across the DM. This emphasizes the importance of accurate measurement techniques

for determining DM thickness and stiffness, particularly in understanding the properties of DM during FED. Addressing this need will be crucial for advancing our understanding and management of corneal disorders and, while also opening avenues for corneal endothelial regeneration medicine open.

Chapter. 6 Future Works

6.1 In Vitro Modelling of Fuchs Endothelial Dystrophy

There is a compelling need for a thorough investigation into the underlying mechanisms that drive the observed cellular responses of Fuchs Endothelial Dystrophy Corneal Endothelial Cells (FED-CECs) to S-guttata pillars. The future work could elucidate the signaling pathways responsible for mediating apoptosis triggered by increased cytoskeletal tension, as was proposed here by the expression of α-SMA and pMLCK. Additionally, it is crucial to conduct an in-depth exploration into the role played by specific cellular contraction molecules and interactions with the extracellular matrix in modulating the cellular response to S-guttata. Further understanding their contributions to early and late-stage FED pathogenesis is essential to develop novel drugs and therapeutics. By undertaking these prospective investigations, researchers can achieve a deeper understanding of FED pathogenesis, thereby laying the groundwork for the development of more effective treatments for FED.

6.2 Characterization of Mechanical Property of Human Descemet's Membrane

Investigations on cell migration on gradient stiffness substrate that mimic DM stiffness will contribute to overarching hypothesis, which the stiffness of DM serves as a critical biophysical cue influencing the behavior of CE progenitor cells, particularly in terms of migration and differentiation processes. A prominent characteristic of FED is the thickening of DM and even in cases where there is no visible protrusion of guttata, it is evident that DM in individuals with FED is thicker compared to normal DM [121]. Investigating the characteristics and thickness of DM could be crucial for gaining a deeper understanding of its involvement in the development and advancement of FED. Since DM stiffness may function as a physio-chemotactic guidance system, directing the migration of cells from the TZ to the peripheral endothelium [31]. The directional

movement of cells towards regions of stiffer ECM, termed "Durotaxis," is believed to play a crucial role in both developmental processes and wound healing [135]. Variations in DM stiffness may affect the migratory behavior of CE progenitor cells. A stiffer DM may enhance cell migration, while a softer DM may inhibit cell movement.

LETTER OF COPYRIGHT PERMISSION

JOHN WILEY AND SONS LICENSE
TERMS AND CONDITIONS

Mar 31, 2024

This Agreement between Springer Nature ("You") and John Wiley and Sons ("John Wiley and Sons") consists of your license details and the terms and conditions provided by John Wiley and Sons and Copyright Clearance Center.

License Number	5759660219121
License date	Mar 31, 2024
Licensed Content Publisher	John Wiley and Sons
Licensed Content Publication	Advanced Healthcare Materials
Licensed Content Title	In Vitro Topographical Model of Fuchs Dystrophy for Evaluation of Corneal Endothelial Cell Monolayer Formation
Licensed Content Author	Evelyn K. F. Yim, Jodhbir S. Mehta, Alon R. Mendez, et al
Licensed Content Date	Oct 4, 2016
Licensed Content Volume	5
Licensed Content Issue	22
Licensed Content Pages	15

Type of use	Dissertation/Thesis
Requestor type	University/Academic
Format	Print and electronic
Portion	Figure/table
Number of figures/tables	2
Will you be translating?	No
Title of new work	In Vitro Modelling of Fuchs Endothelial Dystrophy for Corneal Endothelial Cell Apoptosis and Characterization of Human Descemet's Membrane
Institution name	University of Waterloo
Expected presentation date	Apr 2024
Order reference number	1
Portions	Figure 3, Figure 4
Requestor Location	Myagmartsend Enkhbat 350 Columbia Street West Waterloo, ON N2L 6P8 Canada Attn: John Wiley & Sons
Publisher Tax ID	EU826007151
Total	0.00 USD

TERMS AND CONDITIONS

This copyrighted material is owned by or exclusively licensed to John Wiley & Sons, Inc. or one of its group companies (each a"Wiley Company") or handled on behalf of a society with which a Wiley Company has exclusive publishing rights in relation to a particular work (collectively "WILEY"). By clicking "accept" in connection with completing this licensing transaction, you agree that the following terms and conditions apply to this transaction (along with the billing and payment terms and conditions established by the Copyright Clearance Center Inc., ("CCC's Billing and Payment terms and conditions"), at the time that you opened your RightsLink account (these are available at any time at http://myaccount.copyright.com).

Terms and Conditions

- The materials you have requested permission to reproduce or reuse (the "Wiley Materials") are protected by copyright.
- You are hereby granted a personal, non-exclusive, non-sub licensable (on a stand-alone basis), non-transferable, worldwide, limited license to reproduce the Wiley Materials for the purpose specified in the licensing process. This license, **and any CONTENT (PDF or image file) purchased as part of your order,** is for a one-time use only and limited to any maximum distribution number specified in the license. The first instance of republication or reuse granted by this license must be completed within two years of the date of the grant of this license (although copies prepared before the end date may be distributed thereafter). The Wiley Materials shall not be used in any other manner or for any other purpose, beyond what is granted in the license. Permission is granted subject to an appropriate acknowledgement given to the author, title of the material/book/journal and the publisher. You shall also duplicate the copyright notice that appears in the Wiley publication in your use of the Wiley Material. Permission is also granted on the understanding that nowhere in the text is a previously published source acknowledged for all or part of this Wiley Material. Any third party content is expressly excluded from this permission.
- With respect to the Wiley Materials, all rights are reserved. Except as expressly granted by the terms of the license, no part of the Wiley Materials may be copied, modified, adapted (except for minor reformatting required by the new Publication), translated, reproduced, transferred or distributed, in any form or by any means, and no derivative works may be made based on the Wiley Materials without the prior permission of the respective copyright owner.**For STM Signatory Publishers clearing permission under the terms of the STM Permissions Guidelines only, the terms of the license are extended to include subsequent editions and for editions in other languages, provided such editions are for the work as a whole in situ and does not involve the separate exploitation of the permitted figures or extracts,** You may not alter, remove or suppress in any manner any copyright, trademark or other notices displayed by the Wiley Materials. You may not license, rent, sell, loan, lease, pledge, offer as security, transfer or assign the Wiley Materials on a stand-alone basis, or any of the rights granted to you hereunder to any other

- The failure of either party to enforce any term or condition of this Agreement shall not constitute a waiver of either party's right to enforce each and every term and condition of this Agreement. No breach under this agreement shall be deemed waived or excused by either party unless such waiver or consent is in writing signed by the party granting such waiver or consent. The waiver by or consent of a party to a breach of any provision of this Agreement shall not operate or be construed as a waiver of or consent to any other or subsequent breach by such other party.

- This Agreement may not be assigned (including by operation of law or otherwise) by you without WILEY's prior written consent.

- Any fee required for this permission shall be non-refundable after thirty (30) days from receipt by the CCC.

- These terms and conditions together with CCC's Billing and Payment terms and conditions (which are incorporated herein) form the entire agreement between you and WILEY concerning this licensing transaction and (in the absence of fraud) supersedes all prior agreements and representations of the parties, oral or written. This Agreement may not be amended except in writing signed by both parties. This Agreement shall be binding upon and inure to the benefit of the parties' successors, legal representatives, and authorized assigns.

- In the event of any conflict between your obligations established by these terms and conditions and those established by CCC's Billing and Payment terms and conditions, these terms and conditions shall prevail.

- WILEY expressly reserves all rights not specifically granted in the combination of (i) the license details provided by you and accepted in the course of this licensing transaction, (ii) these terms and conditions and (iii) CCC's Billing and Payment terms and conditions.

- This Agreement will be void if the Type of Use, Format, Circulation, or Requestor Type was misrepresented during the licensing process.

- This Agreement shall be governed by and construed in accordance with the laws of the State of New York, USA, without regards to such state's conflict of law rules. Any legal action, suit or proceeding arising out of or relating to these Terms and Conditions or the breach thereof shall be instituted in a court of competent jurisdiction in New York County in the State of New York in the United States of America and each party hereby consents and submits to the personal jurisdiction of such court, waives any objection to venue in such court and consents to service of process by registered or certified mail, return receipt requested, at the last known address of such party.

WILEY OPEN ACCESS TERMS AND CONDITIONS

Wiley Publishes Open Access Articles in fully Open Access Journals and in Subscription journals offering Online Open. Although most of the fully Open Access journals publish open access articles under the terms of the Creative Commons Attribution (CC BY) License only, the subscription journals and a few of the Open Access Journals offer a choice of Creative Commons Licenses. The license type is clearly identified on the article.

The Creative Commons Attribution License

The Creative Commons Attribution License (CC-BY) allows users to copy, distribute and transmit an article, adapt the article and make commercial use of the article. The CC-BY license permits commercial and non-

Creative Commons Attribution Non-Commercial License

The Creative Commons Attribution Non-Commercial (CC-BY-NC)License permits use, distribution and reproduction in any medium, provided the original work is properly cited and is not used for commercial purposes.(see below)

Creative Commons Attribution-Non-Commercial-NoDerivs License

The Creative Commons Attribution Non-Commercial-NoDerivs License (CC-BY-NC-ND) permits use, distribution and reproduction in any medium, provided the original work is properly cited, is not used for commercial purposes and no modifications or adaptations are made. (see below)

Use by commercial "for-profit" organizations

Use of Wiley Open Access articles for commercial, promotional, or marketing purposes requires further explicit permission from Wiley and will be subject to a fee.

Further details can be found on Wiley Online Library
http://olabout.wiley.com/WileyCDA/Section/id-410895.html

Other Terms and Conditions:

v1.10 Last updated September 2015

Questions? customercare@copyright.com.

person.

- The Wiley Materials and all of the intellectual property rights therein shall at all times remain the exclusive property of John Wiley & Sons Inc, the Wiley Companies, or their respective licensors, and your interest therein is only that of having possession of and the right to reproduce the Wiley Materials pursuant to Section 2 herein during the continuance of this Agreement. You agree that you own no right, title or interest in or to the Wiley Materials or any of the intellectual property rights therein. You shall have no rights hereunder other than the license as provided for above in Section 2. No right, license or interest to any trademark, trade name, service mark or other branding ("Marks") of WILEY or its licensors is granted hereunder, and you agree that you shall not assert any such right, license or interest with respect thereto

- NEITHER WILEY NOR ITS LICENSORS MAKES ANY WARRANTY OR REPRESENTATION OF ANY KIND TO YOU OR ANY THIRD PARTY, EXPRESS, IMPLIED OR STATUTORY, WITH RESPECT TO THE MATERIALS OR THE ACCURACY OF ANY INFORMATION CONTAINED IN THE MATERIALS, INCLUDING, WITHOUT LIMITATION, ANY IMPLIED WARRANTY OF MERCHANTABILITY, ACCURACY, SATISFACTORY QUALITY, FITNESS FOR A PARTICULAR PURPOSE, USABILITY, INTEGRATION OR NON-INFRINGEMENT AND ALL SUCH WARRANTIES ARE HEREBY EXCLUDED BY WILEY AND ITS LICENSORS AND WAIVED BY YOU.

- WILEY shall have the right to terminate this Agreement immediately upon breach of this Agreement by you.

- You shall indemnify, defend and hold harmless WILEY, its Licensors and their respective directors, officers, agents and employees, from and against any actual or threatened claims, demands, causes of action or proceedings arising from any breach of this Agreement by you.

- IN NO EVENT SHALL WILEY OR ITS LICENSORS BE LIABLE TO YOU OR ANY OTHER PARTY OR ANY OTHER PERSON OR ENTITY FOR ANY SPECIAL, CONSEQUENTIAL, INCIDENTAL, INDIRECT, EXEMPLARY OR PUNITIVE DAMAGES, HOWEVER CAUSED, ARISING OUT OF OR IN CONNECTION WITH THE DOWNLOADING, PROVISIONING, VIEWING OR USE OF THE MATERIALS REGARDLESS OF THE FORM OF ACTION, WHETHER FOR BREACH OF CONTRACT, BREACH OF WARRANTY, TORT, NEGLIGENCE, INFRINGEMENT OR OTHERWISE (INCLUDING, WITHOUT LIMITATION, DAMAGES BASED ON LOSS OF PROFITS, DATA, FILES, USE, BUSINESS OPPORTUNITY OR CLAIMS OF THIRD PARTIES), AND WHETHER OR NOT THE PARTY HAS BEEN ADVISED OF THE POSSIBILITY OF SUCH DAMAGES. THIS LIMITATION SHALL APPLY NOTWITHSTANDING ANY FAILURE OF ESSENTIAL PURPOSE OF ANY LIMITED REMEDY PROVIDED HEREIN.

- Should any provision of this Agreement be held by a court of competent jurisdiction to be illegal, invalid, or unenforceable, that provision shall be deemed amended to achieve as nearly as possible the same economic effect as the original provision, and the legality, validity and enforceability of the remaining provisions of this Agreement shall not be affected or impaired thereby.

REFERENCES

1. DelMonte, D.W. and T. Kim, *Anatomy and physiology of the cornea.* J Cataract Refract Surg, 2011. **37**(3): p. 588-98.
2. Doughty, M.J. and M.L. Zaman, *Human corneal thickness and its impact on intraocular pressure measures: a review and meta-analysis approach.* Surv Ophthalmol, 2000. **44**(5): p. 367-408.
3. Gipson, I.K., S.J. Spurr-Michaud, and A.S. Tisdale, *Anchoring fibrils form a complex network in human and rabbit cornea.* Invest Ophthalmol Vis Sci, 1987. **28**(2): p. 212-20.
4. Johnson, D.H., W.M. Bourne, and R.J. Campbell, *The ultrastructure of Descemet's membrane. I. Changes with age in normal corneas.* Arch Ophthalmol, 1982. **100**(12): p. 1942-7.
5. Bourne, W.M., *Clinical estimation of corneal endothelial pump function.* Trans Am Ophthalmol Soc, 1998. **96**: p. 229-39; discussion 239-42.
6. Joyce, N.C., *Proliferative capacity of the corneal endothelium.* Prog Retin Eye Res, 2003. **22**(3): p. 359-89.
7. Bourne, W.M., L.R. Nelson, and D.O. Hodge, *Central corneal endothelial cell changes over a ten-year period.* Invest Ophthalmol Vis Sci, 1997. **38**(3): p. 779-82.
8. Engelmann, K., M. Bohnke, and P. Friedl, *Isolation and long-term cultivation of human corneal endothelial cells.* Invest Ophthalmol Vis Sci, 1988. **29**(11): p. 1656-62.
9. Zhu, C. and N.C. Joyce, *Proliferative response of corneal endothelial cells from young and older donors.* Invest Ophthalmol Vis Sci, 2004. **45**(6): p. 1743-51.
10. Lagali, N., et al., *Laser-scanning in vivo confocal microscopy of the cornea: imaging and analysis methods for preclinical and clinical applications.* Confocal Laser Microscopy—Principles and Applications in Medicine, Biology, and the Food Sciences, 2013.
11. Saikia, P., et al., *Basement membranes in the cornea and other organs that commonly develop fibrosis.* Cell Tissue Res, 2018. **374**(3): p. 439-453.
12. Yurchenco, P.D. and B.L. Patton, *Developmental and pathogenic mechanisms of basement membrane assembly.* Curr Pharm Des, 2009. **15**(12): p. 1277-94.
13. Eghrari, A.O., S.A. Riazuddin, and J.D. Gottsch, *Overview of the Cornea: Structure, Function, and Development.* Prog Mol Biol Transl Sci, 2015. **134**: p. 7-23.
14. Soh, Y.Q., G.S. Peh, and J.S. Mehta, *Evolving therapies for Fuchs' endothelial dystrophy.* Regen Med, 2018. **13**(1): p. 97-115.
15. Chaurasia, S., et al., *Clinical characterization of posterior polymorphous corneal dystrophy in patients of Indian ethnicity.* Int Ophthalmol, 2017. **37**(4): p. 945-952.
16. Patel, S.P. and M.D. Parker, *SLC4A11 and the Pathophysiology of Congenital Hereditary Endothelial Dystrophy.* Biomed Res Int, 2015. **2015**: p. 475392.

17. Darlington, J.K., S.D. Adrean, and I.R. Schwab, *Trends of penetrating keratoplasty in the United States from 1980 to 2004.* Ophthalmology, 2006. **113**(12): p. 2171-5.

18. Wilson, S.E. and W.M. Bourne, *Fuchs' dystrophy.* Cornea, 1988. **7**(1): p. 2-18.

19. Krachmer, J.H., et al., *Corneal endothelial dystrophy. A study of 64 families.* Arch Ophthalmol, 1978. **96**(11): p. 2036-9.

20. Jurkunas, U.V., et al., *Evidence of oxidative stress in the pathogenesis of fuchs endothelial corneal dystrophy.* Am J Pathol, 2010. **177**(5): p. 2278-89.

21. Azizi, B., et al., *p53-regulated increase in oxidative-stress--induced apoptosis in Fuchs endothelial corneal dystrophy: a native tissue model.* Invest Ophthalmol Vis Sci, 2011. **52**(13): p. 9291-7.

22. Miyai, T., et al., *Activation of PINK1-Parkin-Mediated Mitophagy Degrades Mitochondrial Quality Control Proteins in Fuchs Endothelial Corneal Dystrophy.* Am J Pathol, 2019. **189**(10): p. 2061-2076.

23. Matthaei, M., et al., *Fuchs Endothelial Corneal Dystrophy: Clinical, Genetic, Pathophysiologic, and Therapeutic Aspects.* Annu Rev Vis Sci, 2019. **5**: p. 151-175.

24. Kim, E.C., et al., *Screening and Characterization of Drugs That Protect Corneal Endothelial Cells Against Unfolded Protein Response and Oxidative Stress.* Invest Ophthalmol Vis Sci, 2017. **58**(2): p. 892-900.

25. Toyono, T., et al., *MicroRNA-29b Overexpression Decreases Extracellular Matrix mRNA and Protein Production in Human Corneal Endothelial Cells.* Cornea, 2016. **35**(11): p. 1466-1470.

26. Li, Q.J., et al., *The role of apoptosis in the pathogenesis of Fuchs endothelial dystrophy of the cornea.* Arch Ophthalmol, 2001. **119**(11): p. 1597-604.

27. Raviola, G., *Schwalbe line's cells: a new cell type in the trabecular meshwork of Macaca mulatta.* Invest Ophthalmol Vis Sci, 1982. **22**(1): p. 45-56.

28. Hara, S., et al., *Identification and potential application of human corneal endothelial progenitor cells.* Stem Cells Dev, 2014. **23**(18): p. 2190-201.

29. McGowan, S.L., et al., *Stem cell markers in the human posterior limbus and corneal endothelium of unwounded and wounded corneas.* Mol Vis, 2007. **13**: p. 1984-2000.

30. Whikehart, D.R., et al., *Evidence suggesting the existence of stem cells for the human corneal endothelium.* Mol Vis, 2005. **11**: p. 816-24.

31. Yam, G.H., et al., *Characterization of Human Transition Zone Reveals a Putative Progenitor-Enriched Niche of Corneal Endothelium.* Cells, 2019. **8**(10).

32. Gain, P., et al., *Global Survey of Corneal Transplantation and Eye Banking.* JAMA Ophthalmol, 2016. **134**(2): p. 167-73.

33. Tan, D.T., et al., *Corneal transplantation.* Lancet, 2012. **379**(9827): p. 1749-61.

34. Higa, A., et al., *Prevalence of and risk factors for cornea guttata in a population-based study in a southwestern island of Japan: the Kumejima study.* Arch Ophthalmol, 2011. **129**(3): p. 332-6.

35. Kitagawa, K., et al., *Prevalence of primary cornea guttata and morphology of corneal endothelium in aging Japanese and Singaporean subjects.* Ophthalmic Res, 2002. **34**(3): p. 135-8.

36. Lorenzetti, D.W., et al., *Central cornea guttata. Incidence in the general population.* Am J Ophthalmol, 1967. **64**(6): p. 1155-8.

37. Iliff, B.W., S.A. Riazuddin, and J.D. Gottsch, *The genetics of Fuchs' corneal dystrophy.* Expert Rev Ophthalmol, 2012. **7**(4): p. 363-375.

38. Mathews, P., et al., *2022 Eye Banking Statistical Report—Executive Summary.* Eye Banking and Corneal Transplantation, 2023. **2**(3): p. e0008-12.

39. Zhang, J. and D.V. Patel, *The pathophysiology of Fuchs' endothelial dystrophy--a review of molecular and cellular insights.* Exp Eye Res, 2015. **130**: p. 97-105.

40. Borderie, V.M., et al., *Corneal endothelial cell apoptosis in patients with Fuchs' dystrophy.* Invest Ophthalmol Vis Sci, 2000. **41**(9): p. 2501-5.

41. Nanda, G.G. and D.P. Alone, *REVIEW: Current understanding of the pathogenesis of Fuchs' endothelial corneal dystrophy.* Mol Vis, 2019. **25**: p. 295-310.

42. Halilovic, A., et al., *Menadione-Induced DNA Damage Leads to Mitochondrial Dysfunction and Fragmentation During Rosette Formation in Fuchs Endothelial Corneal Dystrophy.* Antioxid Redox Signal, 2016. **24**(18): p. 1072-83.

43. Rizwan, M., et al., *In Vitro Topographical Model of Fuchs Dystrophy for Evaluation of Corneal Endothelial Cell Monolayer Formation.* Adv Healthc Mater, 2016. **5**(22): p. 2896-2910.

44. Mathews, P.M., et al., *Etiology of Global Corneal Blindness and Current Practices of Corneal Transplantation: A Focused Review.* Cornea, 2018. **37**(9): p. 1198-1203.

45. Fuest, M., et al., *Advances in corneal cell therapy.* Regen Med, 2016. **11**(6): p. 601-15.

46. Okumura, N., S. Kinoshita, and N. Koizumi, *Application of Rho Kinase Inhibitors for the Treatment of Corneal Endothelial Diseases.* J Ophthalmol, 2017. **2017**: p. 2646904.

47. Srinivasan, M., et al., *Corticosteroids for bacterial keratitis: the Steroids for Corneal Ulcers Trial (SCUT).* Arch Ophthalmol, 2012. **130**(2): p. 143-50.

48. Camellin, M., *Laser epithelial keratomileusis with mitomycin C: indications and limits.* J Refract Surg, 2004. **20**(5 Suppl): p. S693-8.

49. Liu, C., et al., *Ultraviolet A light induces DNA damage and estrogen-DNA adducts in Fuchs endothelial corneal dystrophy causing females to be more affected.* Proc Natl Acad Sci U S A, 2020. **117**(1): p. 573-583.

50. White, T.L., et al., *Cell cycle re-entry and arrest in G2/M phase induces senescence and fibrosis in Fuchs Endothelial Corneal Dystrophy.* Free Radic Biol Med, 2021. **164**: p. 34-43.

51. Bhogal, M., et al., *Allogeneic Descemet's Membrane Transplantation Enhances Corneal Endothelial Monolayer Formation and Restores Functional Integrity Following Descemet's Stripping.* Invest Ophthalmol Vis Sci, 2017. **58**(10): p. 4249-4260.

52. Okumura, N., et al., *Enhancement of corneal endothelium wound healing by Rho-associated kinase (ROCK) inhibitor eye drops.* Br J Ophthalmol, 2011. **95**(7): p. 1006-9.

53. Haydari, M.N., et al., *A short-term in vivo experimental model for Fuchs endothelial corneal dystrophy.* Invest Ophthalmol Vis Sci, 2012. **53**(10): p. 6343-54.

54. Bostan, C., et al., *In Vivo Functionality of a Corneal Endothelium Transplanted by Cell-Injection Therapy in a Feline Model.* Invest Ophthalmol Vis Sci, 2016. **57**(4): p. 1620-34.

55. Okumura, N., et al., *Enhancement on primate corneal endothelial cell survival in vitro by a ROCK inhibitor.* Invest Ophthalmol Vis Sci, 2009. **50**(8): p. 3680-7.

56. Okumura, N., et al., *The ROCK inhibitor eye drop accelerates corneal endothelium wound healing.* Invest Ophthalmol Vis Sci, 2013. **54**(4): p. 2493-502.

57. Zarouchlioti, C., et al., *Antisense Therapy for a Common Corneal Dystrophy Ameliorates TCF4 Repeat Expansion-Mediated Toxicity.* Am J Hum Genet, 2018. **102**(4): p. 528-539.

58. Bednarz, J., et al., *Immortalization of human corneal endothelial cells using electroporation protocol optimized for human corneal endothelial and human retinal pigment epithelial cells.* Acta Ophthalmol Scand, 2000. **78**(2): p. 130-6.

59. Valtink, M., et al., *Two clonal cell lines of immortalized human corneal endothelial cells show either differentiated or precursor cell characteristics.* Cells Tissues Organs, 2008. **187**(4): p. 286-94.

60. Yokoi, T., et al., *Establishment of functioning human corneal endothelial cell line with high growth potential.* PLoS One, 2012. **7**(1): p. e29677.

61. Sakakura, S., et al., *Non-apoptotic regulated cell death in Fuchs endothelial corneal dystrophy.* Regen Ther, 2023. **24**: p. 592-601.

62. Ziaei, A., et al., *Sulforaphane decreases endothelial cell apoptosis in fuchs endothelial corneal dystrophy: a novel treatment.* Invest Ophthalmol Vis Sci, 2013. **54**(10): p. 6724-34.

63. Ong Tone, S., et al., *Increased Corneal Endothelial Cell Migration in Fuchs Endothelial Corneal Dystrophy: A Live Cell Imaging Study.* Ophthalmol Sci, 2021. **1**(1): p. 100006.

64. Kassumeh, S., et al., *Ex vivo excimer laser ablation of cornea guttata and ROCK inhibitor-aided endothelial recolonization of ablated central cornea.* Acta Ophthalmol, 2020. **98**(6): p. e773-e780.

65. Mustonen, R.K., et al., *In vivo confocal microscopy of Fuchs' endothelial dystrophy.* Cornea, 1998. **17**(5): p. 493-503.

66. Ang, M., et al., *Anterior segment optical coherence tomography.* Prog Retin Eye Res, 2018. **66**: p. 132-156.

67. Griffith, M., et al., *Functional human corneal equivalents constructed from cell lines.* Science, 1999. **286**(5447): p. 2169-72.

68. Zaniolo, K., et al., *Culture of human corneal endothelial cells isolated from corneas with Fuchs endothelial corneal dystrophy.* Exp Eye Res, 2012. **94**(1): p. 22-31.

69. Gendron, S.P., et al., *Restoration of Mitochondrial Integrity, Telomere Length, and Sensitivity to Oxidation by In Vitro Culture of Fuchs' Endothelial Corneal Dystrophy Cells.* Invest Ophthalmol Vis Sci, 2016. **57**(14): p. 5926-5934.

70. Schmedt, T., et al., *Telomerase immortalization of human corneal endothelial cells yields functional hexagonal monolayers.* PLoS One, 2012. **7**(12): p. e51427.

71. Okumura, N., et al., *Involvement of ZEB1 and Snail1 in excessive production of extracellular matrix in Fuchs endothelial corneal dystrophy.* Lab Invest, 2015. **95**(11): p. 1291-304.

72. Benischke, A.S., et al., *Activation of mitophagy leads to decline in Mfn2 and loss of mitochondrial mass in Fuchs endothelial corneal dystrophy.* Sci Rep, 2017. **7**(1): p. 6656.

73. Shoham, A., et al., *Oxidative stress in diseases of the human cornea.* Free Radic Biol Med, 2008. **45**(8): p. 1047-55.

74. McCluskey, P. and R.J. Powell, *The eye in systemic inflammatory diseases.* Lancet, 2004. **364**(9451): p. 2125-33.

75. Bartakova, A., N.J. Kunzevitzky, and J.L. Goldberg, *Regenerative Cell Therapy for Corneal Endothelium.* Curr Ophthalmol Rep, 2014. **2**(3): p. 81-90.

76. Fujimoto, H., et al., *Quantitative regional differences in corneal endothelial abnormalities in the central and peripheral zones in Fuchs' endothelial corneal dystrophy.* Invest Ophthalmol Vis Sci, 2014. **55**(8): p. 5090-8.

77. Ong Tone, S., et al., *Fuchs endothelial corneal dystrophy: The vicious cycle of Fuchs pathogenesis.* Prog Retin Eye Res, 2021. **80**: p. 100863.

78. Crouzet, E., et al., *Tissue engineered endothelial keratoplasty in rabbit: tips and tricks.* Acta Ophthalmol, 2022. **100**(6): p. 690-699.

79. Peh, G.S.L., et al., *Regulatory Compliant Tissue-Engineered Human Corneal Endothelial Grafts Restore Corneal Function of Rabbits with Bullous Keratopathy.* Sci Rep, 2017. **7**(1): p. 14149.

80. Numa, K., et al., *Five-Year Follow-up of First 11 Patients Undergoing Injection of Cultured Corneal Endothelial Cells for Corneal Endothelial Failure.* Ophthalmology, 2021. **128**(4): p. 504-514.

81. Ong, H.S., M. Ang, and J.S. Mehta, *Evolution of therapies for the corneal endothelium: past, present and future approaches.* Br J Ophthalmol, 2021. **105**(4): p. 454-467.

82. Eghrari, A.O. and J.D. Gottsch, *Fuchs' corneal dystrophy.* Expert Rev Ophthalmol, 2010. **5**(2): p. 147-159.

83. Chiou, A.G., et al., *Confocal microscopy in cornea guttata and Fuchs' endothelial dystrophy.* Br J Ophthalmol, 1999. **83**(2): p. 185-9.

84. Hoyt, C., et al., *British Journal of Ophthalmclogy.* British Journal of Ophthalmclogy, 2005. **89**(7).

85. Waring, G.O., 3rd, M.M. Rodrigues, and P.R. Laibson, *Corneal dystrophies. II. Endothelial dystrophies.* Surv Ophthalmol, 1978. **23**(3): p. 147-68.

86. Levy, S.G., et al., *The composition of wide-spaced collagen in normal and diseased Descemet's membrane.* Curr Eye Res, 1996. **15**(1): p. 45-52.

87. Biswas, S., et al., *Missense mutations in COL8A2, the gene encoding the alpha2 chain of type VIII collagen, cause two forms of corneal endothelial dystrophy.* Hum Mol Genet, 2001. **10**(21): p. 2415-23.

88. Muhammad, R., et al., *Micro- and nano-topography to enhance proliferation and sustain functional markers of donor-derived primary human corneal endothelial cells.* Acta Biomater, 2015. **19**: p. 138-48.

89. Vemuganti, G.K., V.M. Rathi, and S.I. Murthy, *Histological landmarks in corneal dystrophy: pathology of corneal dystrophies.* Dev Ophthalmol, 2011. **48**: p. 24-50.

90. Zoega, G.M., et al., *The 7-year cumulative incidence of cornea guttata and morphological changes in the corneal endothelium in the Reykjavik Eye Study.* Acta Ophthalmol, 2013. **91**(3): p. 212-8.

91. Kitagawa, K., et al., *Twenty-three cases of primary cornea guttata.* Jpn J Ophthalmol, 2001. **45**(1): p. 93-8.

92. Yuen, H.K., et al., *A morphologic study of Fuchs dystrophy and bullous keratopathy.* Cornea, 2005. **24**(3): p. 319-27.

93. Yeh, S.I., et al., *In vivo confocal microscopy of combined pre-descemet membrane corneal dystrophy and fuchs endothelial dystrophy.* Cornea, 2011. **30**(2): p. 222-4.

94. Desouza, M., P.W. Gunning, and J.R. Stehn, *The actin cytoskeleton as a sensor and mediator of apoptosis.* Bioarchitecture, 2012. **2**(3): p. 75-87.

95. Kenney, M.C., et al., *Characterization of the Descemet's membrane/posterior collagenous layer isolated from Fuchs' endothelial dystrophy corneas.* Exp Eye Res, 1984. **39**(3): p. 267-77.

96. Bystrom, B., et al., *Laminins in normal, keratoconus, bullous keratopathy and scarred human corneas.* Histochem Cell Biol, 2007. **127**(6): p. 657-67.

97. Ljubimov, A.V., et al., *Extracellular matrix and Na+,K+-ATPase in human corneas following cataract surgery: comparison with bullous keratopathy and Fuchs' dystrophy corneas.* Cornea, 2002. **21**(1): p. 74-80.

98. MJ, H., *Fuchs' endothelial dystrophy of the cornea.* Am J Ophthalmol, 1974. **78**: p. 363-383.

99. Sebbagh, M., et al., *Caspase-3-mediated cleavage of ROCK I induces MLC phosphorylation and apoptotic membrane blebbing.* Nat Cell Biol, 2001. **3**(4): p. 346-52.

100. Song, Y., B.Q. Hoang, and D.D. Chang, *ROCK-II-induced membrane blebbing and chromatin condensation require actin cytoskeleton.* Exp Cell Res, 2002. **278**(1): p. 45-52.

101. Atencia, R., A. Asumendi, and M. Garcia-Sanz, *Role of cytoskeleton in apoptosis.* Vitam Horm, 2000. **58**: p. 267-97.

102. Elmore, S., *Apoptosis: a review of programmed cell death.* Toxicol Pathol, 2007. **35**(4): p. 495-516.

103. Zhang, Y., et al., *Plasma membrane changes during programmed cell deaths.* Cell Res, 2018. **28**(1): p. 9-21.

104. Ndozangue-Touriguine, O., J. Hamelin, and J. Breard, *Cytoskeleton and apoptosis.* Biochem Pharmacol, 2008. **76**(1): p. 11-8.

105. Hinz, B., et al., *Alpha-smooth muscle actin expression upregulates fibroblast contractile activity.* Mol Biol Cell, 2001. **12**(9): p. 2730-41.

106. Hinz, B., *Formation and function of the myofibroblast during tissue repair.* J Invest Dermatol, 2007. **127**(3): p. 526-37.

107. Wang, J., R. Zohar, and C.A. McCulloch, *Multiple roles of alpha-smooth muscle actin in mechanotransduction.* Exp Cell Res, 2006. **312**(3): p. 205-14.

108. Zhang, J., C.N.J. McGhee, and D.V. Patel, *The Molecular Basis of Fuchs' Endothelial Corneal Dystrophy.* Mol Diagn Ther, 2019. **23**(1): p. 97-112.

109. Wang, Z., et al., *Advanced glycation end products and receptors in Fuchs' dystrophy corneas undergoing Descemet's stripping with endothelial keratoplasty.* Ophthalmology, 2007. **114**(8): p. 1453-60.

110. Buddi, R., et al., *Evidence of oxidative stress in human corneal diseases.* J Histochem Cytochem, 2002. **50**(3): p. 341-51.

111. Katikireddy, K.R., et al., *NQO1 downregulation potentiates menadione-induced endothelial-mesenchymal transition during rosette formation in Fuchs endothelial corneal dystrophy.* Free Radic Biol Med, 2018. **116**: p. 19-30.

112. Miyajima, T., et al., *NQO1 downregulation generates genotoxic DNA adducts in in vitro FECD model.* Investigative ophthalmology & visual science, 2019. **60**(9): p. 2177-2177.

113. Gaikwad, N.W., E.G. Rogan, and E.L. Cavalieri, *Evidence from ESI-MS for NQO1-catalyzed reduction of estrogen ortho-quinones.* Free Radic Biol Med, 2007. **43**(9): p. 1289-98.

114. Zahid, M., et al., *Inhibition of catechol-O-methyltransferase increases estrogen-DNA adduct formation.* Free Radic Biol Med, 2007. **43**(11): p. 1534-40.

115. Chi, H.H., C.C. Teng, and H.M. Katzin, *Histopathology of primary endothelial-epithelial dystrophy of the cornea.* Am J Ophthalmol, 1958. **45**(4 Pt 1): p. 518-35.

116. He, Z., et al., *Revisited microanatomy of the corneal endothelial periphery: new evidence for continuous centripetal migration of endothelial cells in humans.* Stem Cells, 2012. **30**(11): p. 2523-34.

117. Palchesko, R.N., et al., *In vitro expansion of corneal endothelial cells on biomimetic substrates.* Sci Rep, 2015. **5**: p. 7955.

118. Gouveia, R.M., et al., *Assessment of corneal substrate biomechanics and its effect on epithelial stem cell maintenance and differentiation.* Nat Commun, 2019. **10**(1): p. 1496.

119. Iwamoto, T. and A.G. DeVoe, *Electron microscopic studies on Fuchs'combined dystrophy. I. Posterior portion of the cornea.* Invest Ophthalmol, 1971. **10**(1): p. 9-28.

120. Amit, C., et al., *Probing the effect of matrix stiffness in endocytic signalling pathway of corneal epithelium.* Biochem Biophys Res Commun, 2020. **525**(2): p. 280-285.

121. Xia, D., et al., *The Ultrastructures and Mechanical Properties of the Descement's Membrane in Fuchs Endothelial Corneal Dystrophy.* Sci Rep, 2016. **6**: p. 23096.

122. Last, J.A., et al., *Determining the mechanical properties of human corneal basement membranes with atomic force microscopy.* J Struct Biol, 2009. **167**(1): p. 19-24.

123. Zoega, G.M., et al., *Prevalence and risk factors for cornea guttata in the Reykjavik Eye Study.* Ophthalmology, 2006. **113**(4): p. 565-9.

124. Xia, D., et al., *Hydrated human corneal stroma revealed by quantitative dynamic atomic force microscopy at nanoscale.* ACS Nano, 2014. **8**(7): p. 6873-82.

125. Morgan, J.T., et al., *Robust and artifact-free mounting of tissue samples for atomic force microscopy.* Biotechniques, 2014. **56**(1): p. 40-2.

126. Lawrence, J., T. Neu, and G. Swerhone, *Application of multiple parameter imaging for the quantification of algal, bacterial and exopolymer components of microbial biofilms.* Journal of Microbiological Methods, 1998. **32**(3): p. 253-261.

127. Korber, D., et al., *Analysis of spatial variability within Mot+ and Mot− Pseudomonas fluorescens biofilms using representative elements.* Biofouling, 1993. **7**(4): p. 339-358.

128. Kolisch, G., et al., *A new approach to improve sludge dewatering using a semi-continuous hydraulic press system.* Water Sci Technol, 2005. **52**(10-11): p. 211-8.

129. Schmid, T., et al., *Biofilm monitoring by photoacoustic spectroscopy.* Water Sci Technol, 2003. **47**(5): p. 25-9.

130. Blauert, F., H. Horn, and M. Wagner, *Time-resolved biofilm deformation measurements using optical coherence tomography.* Biotechnol Bioeng, 2015. **112**(9): p. 1893-905.

131. Wang, X.D. and O.S. Wolfbeis, *Fiber-Optic Chemical Sensors and Biosensors (2013-2015).* Anal Chem, 2016. **88**(1): p. 203-27.

132. Pereira, A., J. Mendes, and L.F. Melo, *Using nanovibrations to monitor biofouling.* Biotechnol Bioeng, 2008. **99**(6): p. 1407-15.

133. Wolf, G., J.G. Crespo, and M.A. Reis, *Optical and spectroscopic methods for biofilm examination and monitoring*. 2002, Springer.

134. Lin, R.C., et al., *Group index of the human cornea at 1.3-microm wavelength obtained in vitro by optical coherence domain reflectometry.* Opt Lett, 2004. **29**(1): p. 83-5.

135. Plotnikov, S.V. and C.M. Waterman, *Guiding cell migration by tugging.* Curr Opin Cell Biol, 2013. **25**(5): p. 619-26.

APPENDIX

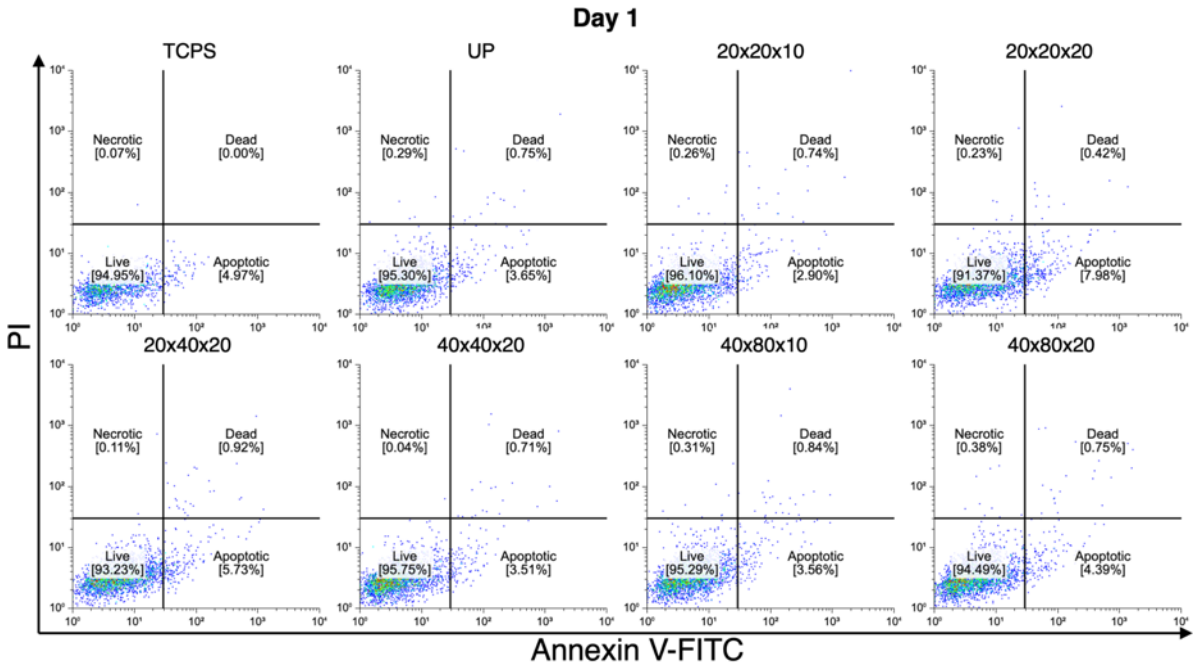


Figure A1. Assessment of S-guttata induced apoptosis using Annexin V and propidium iodide (PI) staining by flow cytometry after one day with high cell density.
Representative flow cytometry scatter plot showing the distribution of cells based on Annexin V and PI staining. Quadrant gates were set to define live (Annexin V^-/PI^-), early apoptotic (Annexin V^+/PI^-), late apoptotic/necrotic (Annexin V^+/PI^+), and necrotic (Annexin V^-/PI^+) populations. Data analyzed from three independent experiment (n = 3). TCPS = Tissue culture polystyrene; UP = unpatterned hot embossed polystyrene.

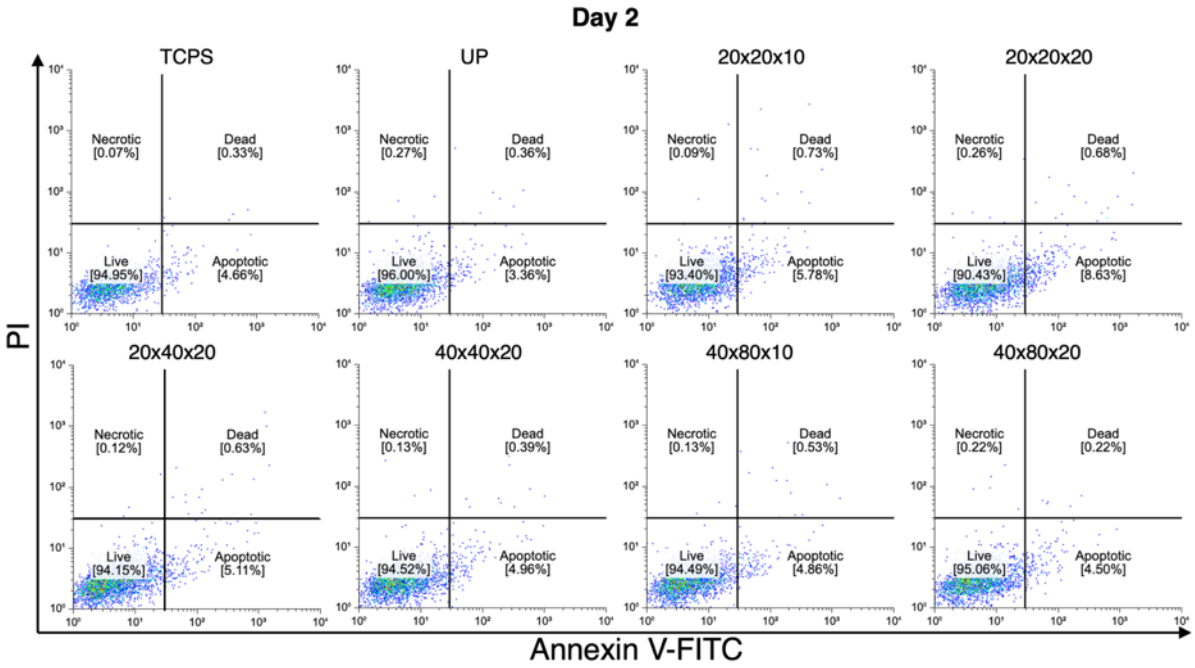


Figure A2. Assessment of S-guttata induced apoptosis using Annexin V and propidium iodide (PI) staining by flow cytometry after two days with high cell density.

Representative flow cytometry scatter plot showing the distribution of cells based on Annexin V and PI staining. Quadrant gates were set to define live (Annexin V^-/PI^-), early apoptotic (Annexin V^+/PI^-), late apoptotic/necrotic (Annexin V^+/PI^+), and necrotic (Annexin V^-/PI^+) populations. Data analyzed from three independent experiment (n = 3). TCPS = Tissue culture polystyrene; UP = unpatterned hot embossed polystyrene.



Figure A3. Brightfield imaging of representative DM CE, PE and TZ regions for gender comparison.

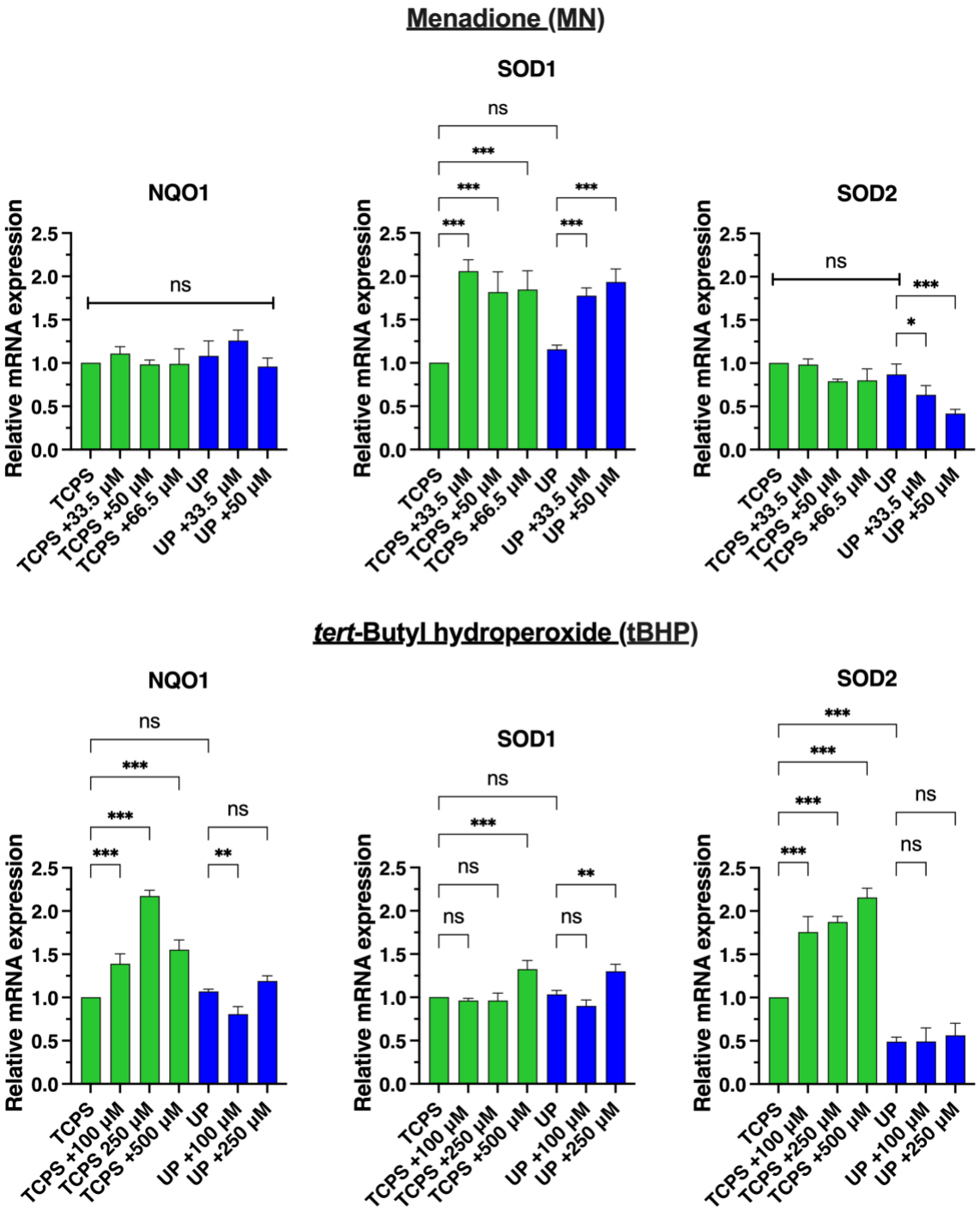


Figure A4. Relative mRNA expression of NQO1, SOD1 and SOD2 genes on TCPS and UP with menadione and tert-Butyl hydroperoxide following two days for titration assay.
RT-qPCR analysis showed expressions relative to TCPS and compared to UP control for NQO1, SOD1, and SOD2 genes. Data were normalized to HPRT1 expression. One, two and three symbols indicate $p < 0.05$, 0.01, and 0.001, respectively. Data are presented as mean ± standard deviation ($n = 3$). UP = unpatterned hot embossed polystyrene.

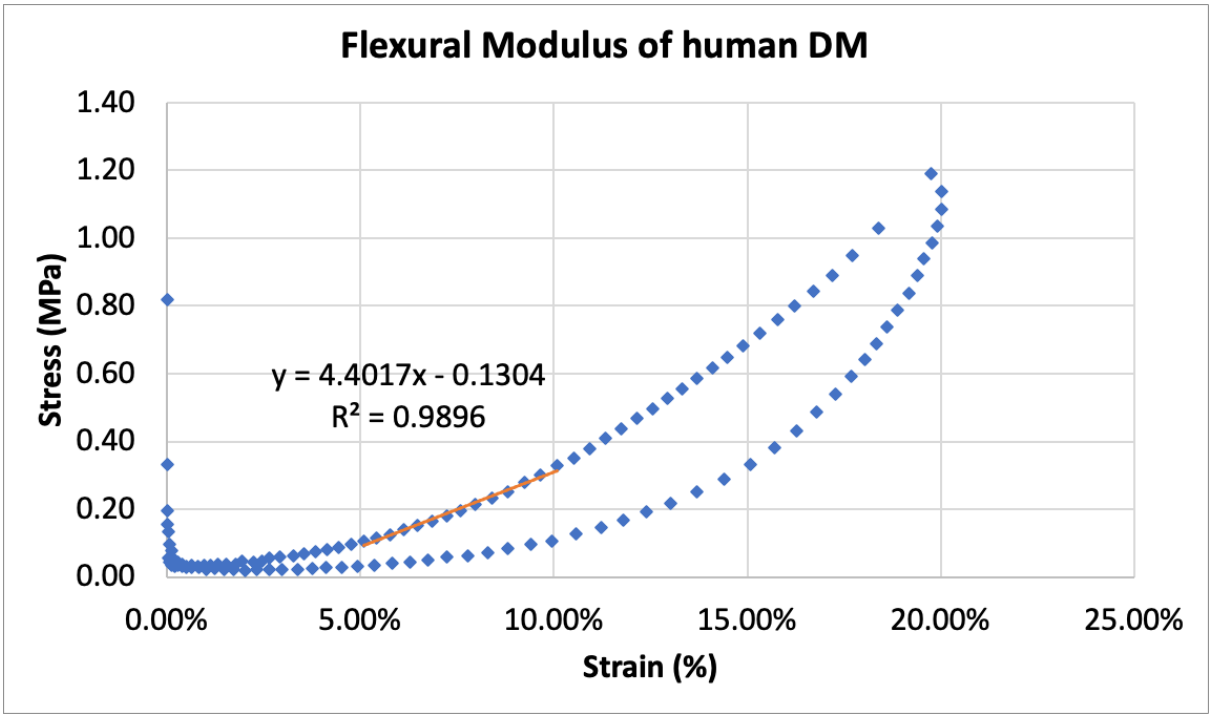


Figure A5. Representative Strain-stress curve of human DM.